Constraining lowermost mantle anisotropy with body waves: A synthetic modeling study

Neala Creasy[1*], Angelo Pisconti[2], Maureen D. Long[1], Christine Thomas[2], and James Wookey[3]

[1]Department of Geology and Geophysics, Yale University
[2]Institut für Geophysik, Universität Münster
[3]Department of Earth Sciences, University of Bristol
*Corresponding author. Email: neala.creasy@yale.edu

Summary

Different mechanisms have been proposed as explanations for seismic anisotropy at the base of the mantle, including crystallographic preferred orientation of various minerals (bridgmanite, post-perovskite, and ferropericlase) and shape preferred orientation of elastically distinct materials such as partial melt. Investigations of the mechanism for D" anisotropy usually yield ambiguous results, as seismic observations rarely (if ever) uniquely constrain a mechanism or orientation and usually rely on significant assumptions to infer flow patterns in the deep mantle. Observations of shear wave splitting and polarities of SdS and PdP reflections off the D" discontinuity are among our best tools for probing D" anisotropy; however, currently available datasets cannot constrain one unique scenario among those suggested by the mineral physics literature. In this work, we determine via a forward modeling approach what combinations of body wave phases (e.g. SKS, SKKS, and ScS) are required to uniquely constrain a mechanism for D" anisotropy. We test nine models based on single-crystal and polycrystalline elastic tensors provided by mineral physics studies. Our modeling predicts fast shear wave splitting directions for SKS, SKKS, and ScS phases, as well as polarities of P and S wave reflections off the D" interface, for a range of propagation directions, via solution of the Christoffel equation. We run tests using randomly selected synthetic datasets based on a given starting model, controlling the total number of measurements, the azimuthal distribution, and the type of seismic phases. For each synthetic dataset, we search over all possible elastic tensors and orientations to determine which are consistent with the synthetic data. Overall, we find it difficult to uniquely constrain the mechanism for anisotropy with a typical number of seismic anisotropy measurements (based on currently available studies) with only one measurement technique (SKS, SKKS, ScS, or reflection polarities). However, datasets that

include SKS, SKKS, and ScS measurements, or a combination of shear wave splitting and reflection polarity measurements, increase the probability of uniquely constraining the starting model and its orientation. Based on these findings, we identify specific regions (i.e., North America, northwestern Pacific, and Australia) of the lowermost mantle with sufficient raypath coverage for a combination of measurement techniques.

Abbreviated Title: Constraining lowermost mantle anisotropy

Keywords (up to 6):

- Seismic anisotropy
- Composition and structure of the mantle
- Mantle processes
- Statistical seismology

1. Introduction

Mantle convection finds its surface expression in plate tectonics and represents a crucial dynamic process in the deep Earth. Despite its importance, the pattern of mantle convection and the forces that drive mantle flow remain imperfectly understood. This is particularly true for the deepest mantle: flow at the base of the mantle likely influences (and/or is influenced by) structures such as large low shear velocity provinces (LLSVPs). Subducting slabs likely penetrate into the lower mantle and hot mantle plumes generate from or near the LLSVPs, indicating a strong connection between the surface and deep mantle processes (e.g., Garnero et al., 2016).

Observations of seismic anisotropy have the potential to illuminate mantle flow, due to the relationship between strain due to mantle convection and seismic anisotropy via lattice preferred orientation (LPO) or shape preferred orientation (SPO) mechanisms. The presence of anisotropy in the D" layer at the base of the mantle has been known for several decades (e.g., Lay and Helmberger, 1983) from the analysis of body wave phases (as summarized in Nowacki et al., 2011). At this point a relatively small fraction (Figure 1) of the core mantle boundary region has been explored for D" anisotropy using body waves. Figure 1 shows a map, updated from Nowacki et al. (2011) illustrating the geographical coverage of previous studies (including recent work by Creasy et al., 2017, Deng et al., 2017, Simmons et al., 2015, Ford et al., 2015, Long and Lynner, 2015, Lynner and Long, 2014, Cottaar and Romanowicz, 2013, and Thomas et al., 2011). Despite these observations, however, we still do not fully understand the anisotropy in these regions. Several different models for D” anisotropy have been proposed, including those that invoke LPO of bridgmanite (Br), post-perovskite (Ppv), or ferropericlase (Fp), and those that invoke SPO of partial melt (see Nowacki et al., 2011 for a review). The mechanisms

responsible for D" anisotropy, the dominant slip systems involved, the orientation of the anisotropic fabric, and the implications for mantle flow geometries thus remain poorly understood.

A variety of body waves has been used to study anisotropy in the deepest mantle. Specifically, direct S, ScS, and Sdiff have been used to observe lowermost mantle anisotropy by measuring shear wave splitting (e.g., Wookey et al., 2005a, Cottaar and Romanowicz, 2013, Thomas et al., 2007, Ford et al., 2006). Combinations of phases, such as SKS-SKKS (e.g., Wang and Wen, 2007; Long, 2009) or S-ScS (e.g., Wookey et al., 2005a; Nowacki et al., 2010), are often useful to isolate the lowermost mantle contribution to splitting. Thomas et al. (2011) used an array analysis technique to observe reflected P and S waves off the D" discontinuity; the azimuthal dependence of the polarity of D" reflections SdS and PdP contains information about lowermost mantle anisotropy. While body wave observations have been extensively used to study anisotropy at the base of the mantle, such studies suffer from the fundamental limitation of small azimuthal coverage; most studies are essentially restricted to a single raypath, which means that the geometry of anisotropy cannot be tightly constrained.

Several recent studies of deep mantle anisotropy have ameliorated this limitation by targeting regions of D" that are sampled by body waves over multiple azimuths (pink regions in Figure 1). These include studies of the lowermost mantle beneath Siberia (Wookey and Kendall, 2008; Thomas et al., 2011), North America (Nowacki et al., 2010), the Afar region of Africa (Ford et al., 2015), and Australia and New Zealand (Creasy et al., 2017). In some cases, one can test whether the observations could clearly distinguish among different mechanisms for anisotropy. For example, Ford et al. (2015) and Creasy et al. (2017) carried out forward modeling of ScS, SKS, and SKKS splitting datasets over

multiple azimuths to test whether a unique mechanism for anisotropy and/or a unique orientation of an assumed mechanism could be identified. In each of these studies it was found that LPO of Ppv matches the observations, but other mechanisms (such as LPO of Br or Fp) were also consistent with the data. None of the studies summarized in Figure 1 has successfully identified a uniquely constrained mechanism or orientation for anisotropy. Motivated by this, we attempt here to understand what observations are needed to distinguish the various possible models for D" anisotropy.

The goal of this study is to understand what combination of body wave datasets (SKS, SKKS, ScS, and reflection polarities) are necessary to uniquely constrain the mechanism and geometry of anisotropy in the lowermost mantle using observations of shear wave splitting and D" reflection polarities. Such an understanding will aid in the design of future observational studies to maximize the chances of uniquely constraining a mechanism. We are interested in understanding the characteristics of datasets that are best suited to constrain the details of D" anisotropy, including the number of measurements needed, the optimal azimuthal coverage, and the optimal combinations of body wave phases. We address two specific questions: 1) What types of datasets (potentially including SKS, SKKS, and/or ScS splitting, and/or reflection polarities) are needed to uniquely identify the causative mechanism for anisotropy (e.g., LPO of Ppv, Br, Fp, or SPO of partial melt)? and 2) if we assume that the mechanism for anisotropy is known to be LPO of Ppv, what type of datasets are needed to uniquely constrain the orientation of the anisotropy?

We carry out forward modeling tests for a suite of synthetic body wave data. Our approach to forward modeling of synthetic datasets follows our previous work on observations of shear wave splitting in D" (Ford et al., 2015; Creasy et al., 2017) and also incorporates measurements of D" polarities of P and S wave reflections (Thomas et al.,

123 2011a). Our approach is to test a variety of candidate elastic tensors that describe various
124 mechanisms for lowermost mantle anisotropy. For each model, we randomly generate more
125 than 5,000 unique synthetic datasets (for SKS, SKKS, and ScS shear wave splitting, plus
126 PdP and SdS polarities) with a certain set of characteristics (e.g., number and type of
127 measurements, as described below) and a random azimuthal distribution. For each set of
128 random raypaths, we compute a set of predicted "observations" of shear wave splitting
129 and/or reflection polarities using a ray theoretical approach. We then attempt to determine
130 what characteristics of body wave datasets are optimal for uniquely constraining anisotropy
131 in the lowermost mantle.
132
133 **2. Methods**
134 2.1 Candidate models for D" anisotropy
135 We first consider which plausible models for D" anisotropy should be tested. The
136 lower mantle is likely composed of pyrolite (e.g., Lee et al., 2004), a model composition
137 that consists of ~76 mol% of bridgmanite (Br: $MgSiO_3$), ~17 mol% of periclase (Fp:
138 (Mg,Fe)O), and ~7 mol% of calcium perovskite (Capv: $CaSiO_3$). In the D" layer at the base
139 of the mantle, we expect a phase change of Br to post-perovskite (Ppv: $MgSiO_3$) (e.g.,
140 Murakami et al., 2004). Based on *ab initio* calculations and laboratory experiments, Br, Fp,
141 and Ppv all have strong single-crystal anisotropy, with Fp being the weakest mineral and
142 the most anisotropic (as summarized in Nowacki et al., 2011), although it is less abundant
143 than Br/Ppv. This suggests that LPO development in any of the dominant lowermost mantle
144 minerals may contribute to the observed anisotropy, as long as deformation is taking place
145 in the dislocation creep regime (e.g., McNamara et al., 2001). Another possible mechanism
146 is aligned pockets of an elastically distinct material such as partial melt in configurations

such as disks, tubes, or sheets, creating shape preferred orientation (SPO) (e.g., Kendall and Silver, 1998) (Tables 1 and 2).

We test a suite of models that describe single-crystal elasticity of lowermost mantle materials derived from *ab initio* calculations, following our previous modeling work (Ford et al., 2015; Creasy et al., 2017). This approach assumes that an aggregate will have the same anisotropic geometry (although not strength) as a single crystal. In addition to the single-crystal models, we test one model (for Fp LPO) based on deformation experiments (Long et al., 2006) and models that invoke the SPO (shape-preferred orientation) of partial melt (Table 1), with elastic constants calculated using an implementation of effective medium theory within the MSAT toolbox (Walker and Wookey, 2012).

Finally, our last candidate model approximates a textured Ppv aggregate and is derived from a 3D, global mantle flow field calculation in combination with a visco-plastic self-consistent model LPO development in Ppv (Walker et al., 2011). We determined a representative elastic tensor for Ppv texture development in high-strain simple shear by querying the TX2008.V1.P010 model of Walker et al. (2011), which combined a lower mantle viscosity model from Mitrovica and Forte (2004) with a mantle density model from Simmons et al. (2009). We only considered the case in which slip on the (010) plane dominates; this is the most likely slip plane for Ppv based on experiments (Walte et al., 2009; Yamazaki et al., 2006), modeling (Goryaeva et al., 2017), and observations of D" anisotropy (Creasy et al., 2017; Ford et al., 2015; Thomas et al., 2011). To obtain a representative average tensor for simple shear, we identified a 15° by 15° geographical region of the global flow (beneath the northern Atlantic Ocean) that is dominated by strong horizontal shear. We then extracted the 16 elastic tensors (the model calculated tensors

every 5°) from the resulting TX2008.V1.P010 elasticity predictions in this region averaged them.

2.2 Computation of reflection polarities and fast splitting directions

Given the full suite of candidate models for elasticity in D" to be used in our study (Table 1), we implement methods for predicting various types of body wave observations for these scenarios. We calculated predicted shear wave splitting fast directions for SKS, SKKS, and ScS phases (Figure 2) over a range of azimuths (every 5°) and inclinations for each of these models (Tables 1) by solving the Christoffel equation using the MSAT toolkit of Walker and Wookey (2012). The three different phases propagate at different inclination angles: ~55°, 35°, 0° from the horizontal, respectively.

We then calculated the reflection polarities of SdS and PdP and the corresponding predicted shear wave splitting fast directions (Figure 3) over a range of azimuths (every 5°) and inclinations for each of these models (Tables 1 and 2). Table 2 summarizes the models used to generate predictions of D" reflection polarities (SdS and PdP), including the assumed slip system, based on the methodology of Thomas et al. (2011). These models were constructed by assuming horizontal simple shear at the base of the mantle, where the dominant slip direction aligns parallel to the CMB, the slip plane is assumed to be horizontal, and 12% of the aligned single crystals are mixed linearly with its isotropic equivalent. This choice of 12% alignment was based on the previous work of Thomas et al. (2011), and yields reasonable anisotropic strengths; since we focus on reflection polarities and not amplitudes, however, this choice of value is not critical. We assume that the aligned grains are sub-parallel with the slip direction and the slip plane is sub-parallel to the CMB and the remaining grains are randomly oriented for Models A, B, and C (Figure

194 3). We tested three models (Models A [Ppv], C [Br], and D [Fp] in Table 2) in which the
195 D" discontinuity represents a change in alignment of the mineral grains from an isotropic
196 (above the discontinuity) to an anisotropic (below the discontinuity) regime. In Model B,
197 the D” discontinuity is an isotropic phase transformation from Br to anisotropic Ppv. The
198 predicted values for reflection polarities for each model are shown in Figure 3 and were
199 calculated using Guest and Kendall (1993) from the velocity perturbation and reflection
200 coefficients at the interface between an isotropic and anisotropic layer with respect to
201 azimuth from the dominant slip direction and epicentral distance (Thomas et al., 2011).
202 Our approach to calculating predicted shear wave splitting parameters and
203 reflection polarities for our synthetic models makes several simplifying assumptions. First,
204 we only directly model shear wave splitting due to lowermost mantle anisotropy, and
205 ignore any potential contributions from the upper mantle. Our approach therefore assumes
206 that any upper mantle contribution (in real data) has been correctly accounted for; we
207 further assume that the bulk of the lower mantle is isotropic (Meade et al., 1995). We do
208 not explicitly consider how incorrect upper mantle corrections could bias the resulting D”
209 observations, which is beyond the scope of our study. Second, we rely on ray theory and
210 do not consider finite frequency wave effects in our modeling. Ray theoretical predictions
211 are generally adequate for homogenous regions of D” (e.g., Nowacki and Wookey, 2016),
212 although they may break down for laterally heterogeneous anisotropic models
213 (heterogeneities varying over hundreds of km). Third, in our modeling we approximate the
214 propagation directions for SKS and SKKS with average inclination angles for these phases,
215 and for ScS we assume that propagation is horizontal through the D” layer. This assumption
216 follows previous work (Nowacki et al., 2010; Ford et al., 2015; Creasy et al., 2017). In the
217 Earth and at the relevant epicentral distances, ScS can be inclined from the horizontal up

to ~15°, but this assumption has only a modest effect on the predicted splitting parameters. We assume the three different phases (SKS, SKKS, and ScS) propagate at different inclination angles: ~55°, 35°, 0° from the horizontal, respectively. Inclination angles are based on a straight-line approximation, calculated using TauP (Crotwell et al., 1999) based on the PREM Earth model (Dziewonski and Anderson, 1980) for distances of 90° - 120° for SKS/SKKS and 60° - 80° for ScS with an event at a depth 10 km. We use these average propagation angles for SKS and SKKS in our modeling for simplicity, although for real data they can vary by up to 10° - 20° from these average values.

2.3 Modeling approach and strategy

Our goal is to conduct a series of stochastic forward modeling simulations to test whether we can uniquely constrain a given starting model (an elastic tensor) and its orientation using a dataset with a given set of characteristics (e.g., number and type of measurements, azimuthal distribution). Our forward modeling framework follows Ford et al. (2015), who modeled a shear wave splitting dataset that samples the lowermost mantle beneath the Afar peninsula along the edge of the African LLSVP. We did not consider delay times in our modeling. Individual delay time measurements contain larger error bars, which limit the utility of using the relative travel times in a dataset as a discriminant. The complete tradeoff between fabric strength and layer thickness also limits the utility of using absolute travel times as a constraint.

For each of our modeling experiments, we first choose a starting model and orientation from the possibilities listed in Table 1. As an example, we first consider a horizontally aligned elastic tensor of Ppv with [100] and [010] axes parallel to the CMB, which we will use to illustrate our approach in several of the following figures. Second, we

242 randomly identify a set of raypaths of SKS, SKKS, and/or ScS sometimes in combination
243 with SdS and PdP reflection polarities. Third, we calculate the predicted fast-axis directions
244 and/or reflection polarities of SdS and PdP for each raypath, as described in Section 2.2.

245 In the fourth step, we model the synthetic dataset by applying the same forward
246 modeling technique that we typically use for real data (Ford et al., 2015). Specifically, we
247 treat the synthetic observations as though the actual model used to generate them was not
248 known, and test all possible models listed in Tables 1 and 2) in all possible orientations
249 (every 5°) to identify models/orientations that are consistent with the synthetic dataset. A
250 candidate model/orientation is discarded if the predicted and "observed" fast splitting
251 directions differ by more than 20° or if the predicted reflection polarities are opposite those
252 of the "observations". We apply this 20° cutoff for the splitting observations, based on
253 methods and reasonable estimates of errors in previous shear wave splitting studies (see
254 Ford et al., 2015). While this misfit criterion is appropriate for measurement errors, it does
255 not take into account effects such as inaccurate upper mantle corrections for actual D"
256 anisotropy observations, or the possible finite-frequency effects of complex structure.
257 Explicit consideration of these effects in D" anisotropy studies is a subject of ongoing
258 research. For each candidate model/orientation that was considered an acceptable fit to the
259 synthetic data, we calculated a total misfit value (for the fast polarization directions only)
260 based on a residual sum of squares approach, following Ford et al. (2015). Each fast
261 direction misfit is normalized by the maximum residual of 90° and summed by using the
262 residual sum of squares, in which we calculate the square of the difference between the
263 observation and data prediction.

264 The fifth and final step in our modeling strategy is to repeat the entire process a
265 large number (M) of times for random raypath configurations. All of these steps are

illustrated in Figure 4. In each iteration, we randomly choose a new azimuthal distribution of raypaths for a new synthetic dataset with varying characteristics (such as the number and type of observations, described in more detail below). We report our results by considering what percentage of the M iterations could uniquely identify the starting model. Each individual iteration was designated as "*uniquely constrained*" if it successfully identified the correct starting model, and could completely rule out any other candidate model. However, if there was at least one other anisotropy configuration (any candidate elastic tensor model, in any orientation) was found to be consistent with the synthetic observations, that iteration was designated "*not uniquely constrained*." Therefore, all our model results are characterized through a *%-uniquely constrained* value, which identifies how what percentage of the M simulations could uniquely constrain the starting model. The actual values of these "%-uniquely constrained" estimates are strongly dependent on our modeling choices, and the estimates could change with different modeling assumptions. However, these percentages can be compared across our suite of numerical simulations, since our assumptions are consistent across the various tests.

Within this modeling framework, we tested a series of synthetic dataset characteristics described the following three distinct variables: the number of measurements (N), ratio of the number of SK(K)S (that is, SKS plus SKKS) measurements to the total number of shear wave splitting measurements (we term this ratio the "SKS number"), and the azimuthal distribution of measurements, as quantified by the angular dispersion (R). Angular dispersion is defined as:

$$C_P = \sum_{i=1}^{n} \cos(a_i), \; S_P = \sum_{i=1}^{n} \sin(a_i), \tag{1}$$

$$R = \sqrt{C_P^2 + S_P^2}, \tag{2}$$

where a_i is a vector of directions and R is angular dispersion, which varies from 0 (uniform dispersion) to 1 (concentration in one direction) (Mardia and Jupp, 2000). A graphical definition of R is shown in Supplementary Figure S1.

We tested different combinations of N and SKS number to gain insight into how many measurements, and in what combination, are typically needed to uniquely constrain the anisotropy. For angular dispersion, we calculated the value of R for each of the M iterations carried out in each test; then, we queried the large number of simulations to understand how the azimuthal distribution of the synthetic data affected its ability to constrain anisotropy.

2.4 Distinguishing the mechanism and orientation of anisotropy

For the first round of tests, we sought to understand how many shear wave splitting measurements, and in what combination (as described by the SKS number), are generally needed to uniquely constrain the *mechanism* for anisotropy. That is, we tested whether synthetic datasets could be shown to be consistent *only* with the correct starting model (e.g., Ppv, as opposed to other models listed in Table 1), and with *no other* candidate mechanism. For this round of tests, we used the single crystal models in Table 1 as starting models, each in several different orientations. The LPO model of Ppv was only used for the second round of tests. We defined the starting model orientation via the rotation angle about the [100] axis from the horizontal (note that Figure 2 only shows an example with a horizontal [100] and [010] direction). We arbitrarily tested each single crystal model at three different orientations based on the rotation angle about the [100] axis from the horizontal: 0°, 45°, and 90°. For the LPO model of Ppv, we only test the original orientation for the starting model and do not test a rotated version of the elastic tensor since this model is based on a

region in the Walker et al. (2011) with horizontal shear. In our initial round of tests, we focused only on cases in which shear wave splitting observations of SKS, SKKS, and ScS (for varying N, SKS number, and R values) were used to constrain the models; in later tests, we explored scenarios in which reflection measurements were combined with shear wave splitting data, in order to estimate the improvement obtained by combining different data types.

We also carried out a series of tests whose goal was to constrain the *orientation* of the elastic tensor for the case in which the mechanism for anisotropy is known (or assumed). For this line of inquiry, we focused on Ppv as a test case; we did not test other mechanisms in this part of the study. The choice to focus on Ppv was made for simplicity and because Ppv is often invoked as the preferred mechanisms for anisotropy in D" (Creasy et al., 2017; Ford et al., 2015; Ford and Long, 2015; Nowacki et al., 2010; Thomas et al., 2011a; Wookey et al., 2005b). We consider both single-crystal Ppv tensors and elastic tensors derived from texture modeling, as discussed above. As in our first series of tests, we initially focus on synthetic datasets that only contain shear wave splitting observations, and then examine cases that also include reflection measurements.

Lastly, in addition to the two major lines of inquiry we address in our modeling (what kind of datasets are needed to constrain the *mechanism* and *orientation*) of lowermost mantle anisotropy, we performed two practical tests using horizontal Ppv as a starting model. First, we carried out a test of how many iterations (that is, values of M) are needed for our forward algorithm to converge on an estimate of the probability of identifying unique models. Second, we tested the addition of Gaussian noise to the shear wave splitting predictions, in order to understand how well real, noisy datasets might perform. The results of these practical tests are described below. While seismic data can deviate from a Gaussian

distribution (Groos and Ritter, 2009), we only consider Gaussian distributed noise here since in an ideal case, seismic noise is Gaussian distributed (Bendat and Piersol, 2011).

3. Results

3.1 Illustrative examples: Model runs for a ppv starting model

To illustrate the process and results of our modeling, we discuss here the results from a test that attempts to constrain the *starting model,* as well as one iteration of a test that attempts to constrain the *orientation*. In both cases, we use synthetic shear wave splitting data only. For these examples, as in all of our tests, we follow the five steps of our method outlined above (Figure 4): (1) choose a starting model and orientation, (2) choose the number of observations and the SKS number to randomly generate a distribution of raypaths, (3) calculate the predicted fast polarization directions (of SKS, SKKS, and ScS) and reflection polarities (for SdS and PdP) for the synthetic dataset for the chosen starting model, (4) conduct a forward modeling search over all possible orientations for all possible candidate models to eliminate all models/orientations that do not fit the "observations" using a misfit cutoff. Then, if all other models and orientations can be eliminated by applying the misfit cutoff, this set of synthetic raypaths are able to uniquely constrain the starting model and designated as "*uniquely constrained*." The fifth step would be repeating this process M number of times but for this illustrative example, M = 1.

Our illustrative example is shown in Figure 5. For this example, we chose a starting model of non-rotated Ppv (in this case, the [100] and [010] crystallographic axes are parallel to the CMB) (Figure 5a). In all of our single-crystal elasticity tests, we do not assume a dominant slip system; rather, we invoke a starting orientation in the geographic reference frame identified by the angle of the mineralogical axes. This particular example

involves 9 splitting observations, 6 of which are SK(K)S (that is, an SKS number of 2/3). The randomly generated azimuthal distribution of these chosen phases is shown in Figure 5b. The predicted fast polarization directions for our chosen model and ray configuration, plotted in a ray-centered reference frame, are shown in Figure 5c. A search over all possible candidate models and orientations (rotating every 5°) shows that there is no other model, other than the correct starting model (Ppv), that can match each of the synthetic fast splitting directions to within 20° (our pre-defined misfit cutoff). Put another way, for every possible combination of starting model and orientation (other than the correct, known starting model), at least one predicted fast splitting orientation differed from that in the dataset by more than the 20° misfit cutoff. Since this particular configuration of observations could uniquely identify the starting model and no other models, it is designated "*uniquely constrained*."

This particular example illustrates a single iteration (M = 1) of our testing, but the power of our approach lies in repeating this a large number of times to understand what percentage of randomly generated synthetic datasets have the ability to uniquely constrain the starting model. In order to understand how many iterations are needed to converge on an estimate of this probability, we conducted an "iteration test" for our horizontal Ppv starting model, as shown in Figure 6. For this test, we used 9 shear wave splitting measurements (N = 9) and an SKS number of 2/3, as in the example shown in Figure 5, and ran a large number of iterations (M = 50,000), each involving a new, random distribution of propagation azimuths. After each successive iteration, we calculated the percentage (of M iterations) for which the synthetic dataset was able to *uniquely constrain* the starting model, as shown in Figure 6. For this starting model, after a large number of iterations, we found that 41% of all iterations could uniquely constrain the starting model,

385 while for the other 59% of the raypath configurations, there was another model/orientation
386 that could simulate the synthetic data. Our running estimate of how likely a dataset with 9
387 splitting observations (6 SK(K)S, 3 ScS) converges on an average value of 41% after
388 approximately 1,000 iterations (Figure 5). Based on this iteration test, we have chosen to
389 run each of our numerical experiments for M = 5,000 iterations, balancing computational
390 cost and the need for our estimates to converge.

391 Next, to illustrate our process for testing whether synthetic data can identify a
392 unique starting *orientation*, we show in Figure 6 two examples of searching for the correct
393 starting orientation for the same horizontal Ppv starting model as in Figure 4. For this
394 example, we chose two different raypath configurations, one with N = 8 observations (5
395 SKS+SKKS and 3 ScS; Figure 7a) and one with N = 4 (3 SKS+SKKS and 1 ScS; Figure
396 7b). We assume that the mechanism for anisotropy is known to be Ppv and that the elastic
397 constants are known, and search over all possible orientations to test whether there are
398 additional configurations (other than the known starting orientation) that can reproduce the
399 synthetic observations.

400 Figures 7a and 7b show all possible orientations that satisfy this suitability criterion
401 for each of our two examples (N = 8 and N = 4, respectively), with each orientation color-
402 coded by its calculated misfit value (Equation 1). Following Ford et al. (2015), we search
403 for local minima of misfit within the 3-D rotation space. For our N = 8 case (Figure 7a),
404 the set of 8 measurements could uniquely identify the starting orientation, and would be
405 designated as "uniquely constrained." However, for our N = 4 case (Figure 7b), we
406 identified two other possible orientations (that is, the known correct starting orientation,
407 plus two others). Therefore, for this particular raypath configuration, the solution is

408 designated “not uniquely constrained.” We note, however, that the orientation with the
409 lowest misfit value (magenta dot in Figure 7b) is, in fact, the correct starting orientation.
410 Finally, we illustrate an example calculation that includes Gaussian noise in the
411 synthetic observations (Figure 7c). This test relies on the same horizontal Ppv starting
412 model, and uses the same raypath configuration (N = 4) as the test shown in Figure 7b. The
413 only difference is that when the predicted shear wave splitting fast directions are calculated
414 based on the starting model and raypath distribution, we add Gaussian noise to the fast
415 splitting direction “observations,” with a maximum error excursion of 20° and a standard
416 deviation of 9°. Figure 7c reveals that the case with Gaussian noise produced the same two
417 possible sets orientations as fitting the data, but now the solution with the minimum misfit
418 is not associated with the correct solution.
419
420 3.2 Results: Constraining the anisotropy mechanism
421 Building on the illustrative examples discussed in section 3.1, we now explore the
422 results of a large number of simulations with different starting models and raypath
423 configurations. We first address the question of what kind of datasets are needed to
424 distinguish among the various models listed in Figures 2 and 3. For this suite of numerical
425 experiments, we examined a variety of starting models and orientations, as well as a variety
426 of raypath configurations (as defined by the number of splitting measurements, the SKS
427 number, and the angular dispersion of the raypath azimuths). The results of these
428 experiments are shown in Figure 8. We first examine those model runs that only included
429 shear wave splitting data, shown in the nine panels of Figure 8a.
430 We initially focus on the mechanism and orientation of the starting model (Figure
431 8a, left panels), and explore how the probability of uniquely constraining the mechanism

varies as a function of the number of measurements. For each of the models considered, the probability of identifying the unique starting model increases with the number of measurements, as expected, typically with a sharp increase in the probability for N values between ~6-9. In all cases, approximately 9 measurements are needed in order to have a ~50% chance of constraining the starting model, while a high number of splitting measurements ($N \approx 15$) is needed for the probability to reach ~90%. (For comparison, the datasets of Ford et al. (2015) and Creasy et al. (2017) contained between 4-8 splitting measurements.) The starting model with the highest success rate at constraining the mechanism is Br, as opposed to Fp and Ppv.

The probability of constraining the starting mechanism depends on the orientation of the starting model; as shown in Figure 8a, we tested orientations with a horizontal [100] crystallographic axis, 45° rotated about the [100], and 90° rotated about the [100] axis. Interestingly, for Ppv it is easier to uniquely constrain the starting model in the 90° case; in contrast, for Br the chances are highest for the horizontal case, and for Fp the chances are substantially higher for the tilted case. The reason for this result for Ppv can be discerned by examining the predicted splitting patterns in Figure 2. For the horizontal case, predicted fast splitting directions for ScS do not vary with azimuth; however, if the Ppv tensor is rotated by 90° about the [100] axis, there is significant variation in fast directions with azimuth. With greater variability in the predicted fast polarization directions (lower angular dispersion), there is a higher probability of constraining that model for a given number of ScS observations. A similar principle is at work for Fp: ScS fast directions do not vary with azimuth for either horizontally or vertically aligned Fp, but in the tilted case, variability is present. Generally, the anisotropy scenarios that yield higher chances of uniquely constraining the starting model have lower mean angular dispersion values of the

predicted fast-axis directions (Supplementary Figure S2). Models that have little variation in fast-axis directions with azimuth, such as non-rotated Fp, are more difficult to uniquely constrain (Figure S2c and Figure 8a).

We also examined how the balance between SKS+SKKS vs. ScS phases in the synthetic dataset affected the ability of the synthetic "observations" to uniquely constrain the starting model (Figure 8a, middle panels). For these experiments, we varied the SKS number from 0 (all ScS measurements) to 1 (all SKS+SKKS measurements) for a fixed value of N = 9. For very high or low values of SKS number we find a low probability of uniquely constraining the starting model with substantially higher probabilities for intermediate SKS numbers. The optimal ratio of SK(K)S phases to total measurements differs slightly for different starting models, but in general an SKS number between 0.5 and 0.8 maximizes the chances of constraining the anisotropic mechanism. In all cases, a combination of ScS and SK(K)S shear wave splitting observations, instead of splitting measurements for just one phase type, will drastically improve the probability of constraining the starting model.

Additionally, we explored the importance of how the angular distribution of the synthetic raypaths affected the ability to constrain the starting model, finding only a weak effect (Figure 8a, right panels). As expected, datasets with a wide angular distribution ($R < 0.2$) have the largest probability of uniquely constraining the starting model in all cases. At very large values of angular dispersion ($R > 0.8$), for which the raypaths are clustered over a narrow range of azimuths, the splitting "observations" are sampling similar parts of the elastic tensor. Because of this, datasets that are tightly clustered in azimuth cannot capture the symmetry of the tensor and cannot distinguish among different candidate

mechanisms for anisotropy. For intermediate values of R, the dependence on R is not strong.

Finally, we explored the value of combining shear wave splitting and reflection polarity measurements when trying to uniquely constrain an anisotropic model. Figure 8b shows the results of adding a single reflection polarity measurement (that is, a measurement of PdP and SdS polarities for a single raypath) to a dataset of shear wave splitting measurements. For this test, we considered a smaller number (four) of potential candidate models (as shown in Figure 3), so the probabilities of uniquely constraining the anisotropy mechanism are generally higher than in our other tests. For this test, we chose a raypath configuration involving an SKS number of 0.67 and varied the number of shear wave splitting measurements from 0 to 15. We used a starting model A in Figure 3 (anisotropy due to Ppv), and tested configurations that involved both shear wave splitting measurements and one additional set of reflection polarity measurements (both PdP and SdS) at a single azimuth. This test (Figure 8b) demonstrates that despite the fact that reflectivity measurements provide only binary information (positive or negative polarities), the incorporation of a different data type into the test increases the probability of uniquely constraining the starting model. In some cases, this increase is substantial; specifically, for datasets containing between 4 and 8 shear wave splitting measurements. The addition of reflection polarity data can increase the probability of constraining the starting model by ~10-18% (right panel of Figure 8b).

3.3 Results: Constraining the anisotropy orientation

The tests shown in Figure 8 illustrate the ability of shear wave splitting and reflection polarity data to constrain the anisotropic mechanism if the algorithm is allowed

503 to consider a range of possible models. We now turn our attention to tests in which we
504 assume that the mechanism that creates the anisotropy, as well as the elastic constants
505 associated with that mechanism, are known, but the orientation of the elastic tensor is not
506 known. In general, this is an easier problem than uniquely constraining the starting model,
507 as the observations need not distinguish among different candidate elastic tensors, only
508 among different possible orientations. In practical terms, this type of modeling exercise
509 would be suitable for datasets that sample a region of the lowermost mantle whose
510 mineralogy and temperature conditions can be constrained using independent observations
511 or models (for example, seismic velocities in combination with mineral physics
512 constraints).

513 For this set of tests, we first consider single-crystal Ppv in three different
514 configurations: 1) [100] and [010] axes oriented in the horizontal plane, 2) a 90° rotation
515 about the [100] axis, and 3) randomly chosen orientations. For the third configuration, we
516 randomly identified nine different, unique starting orientations. These randomly generated
517 orientations were used for each of the ~5,000 iterations in this scenario. As with the tests
518 discussed in section 3.2, we tested a variety of raypath configurations with a range of N
519 (number of measurements), SKS number, and examined how our results varied with the
520 angular dispersion characteristics of the synthetic raypaths. The results of our single-crystal
521 Ppv tests are shown in the top row of Figure 9. The results for our collection of nine random
522 starting orientations are shown in detail in Supplementary Figure S3.

523 As expected, our tests demonstrate that uniquely constraining the orientation of the
524 starting model is much easier and requires fewer measurements than uniquely constraining
525 the starting model/mechanism (Figure 7). In general, a ~50% probability of correctly
526 retrieving the anisotropy is achieved with ~6-9 splitting measurements (top left panel of

Figure 9a). The orientation of the starting model does affect the likelihood of uniquely identifying the anisotropy orientation. With our randomly generated starting orientations, the probability of constraining the starting orientation varies (Figure S3), but on average randomly oriented starting models do slightly worse compared to the results shown in Figure 9. For six measurements, the randomly orientated models on average find the correct orientation in 65% of all simulations, compared to Figure 9, where a non-rotated and Ppv rotated by 90° can constrain on average 75% of the simulations. As with our previous tests, it is clear that a mixture of SK(K)S and ScS shear wave splitting measurements provide the highest likelihood of constraining the starting orientation, although the optimal mix of ScS and SK(K)S depends on the starting model orientation. Our tests confirm that datasets that contain only ScS measurements (that is, SKS number of zero) cannot constrain the azimuth of the Ppv elastic tensor if its [100] axis is horizontal, due to the lack of variability in predicted fast polarization direction (Figure 2). The dependence of our results on angular dispersion of the propagation azimuths (right panels of Figure 9a) are similar to those for the case in which we attempted to retrieve the starting model; in general, a wide distribution of azimuths will increase the probability of uniquely constraining the orientation of Ppv, while datasets whose propagation azimuths are tightly clustered are less ideal. The same is generally true for the random starting models, despite some small excursions from the overall trend (Figure S3). These small excursions or "bumps" in the curves are artifacts, and are related to stochastic variations in the distribution of the predicted fast splitting directions for different models.

Next, we considered elasticity models that explicitly take into account texture development in a polycrystalline aggregate, in addition to the single-crystal elastic tensors that are the main focus of our study. While there are many uncertainties in texture models

for Ppv at lowermost mantle conditions, these models may be more representative of a realistic texture of aligned Ppv mineral grains. We only considered one case, invoking dominant slip on the (010) plane. Somewhat surprisingly, we found that for modeled Ppv LPO, there is a much lower probability of constraining the orientation of the elastic tensor than for test cases that used a single crystal elastic tensor (Figure 8a). We investigated possible reasons for this, and found that in contrast to the single-crystal models, for the textured Ppv model it is fairly common for the algorithm to identify what we term as "unstable" solutions, which are illustrated in Figure S4. In this situation, a certain orientation might fit the observations, but adjacent orientations (in which the elastic tensor is rotated by 5°) do not. This is in contrast to the behavior of single-crystal elastic models (Figure 2), in which the best-fitting orientations are adjacent to other solutions that also fit the data (in other words, the misfit values vary smoothly as a function of rotation angles of the candidate tensors). In addition, the presence of unstable solutions is highly dependent on our use of the misfit criterion of 20°. Figure S4 shows results for a range of misfit cutoff values, and demonstrates that these unstable solutions disappear with the application of more conservative misfit criteria.

We define a "stable" solution as one in which, if the elastic tensor is rotated slightly (~5° in any direction), the rotated elastic tensor would still yield an acceptable fit to the synthetic data. In contrast, an "unstable" solution is one that has no adjacent orientations that yield an acceptable fit to the data. For the case of the textured Ppv model, the algorithm generally identifies many "unstable" orientations (Figure 9); again, this is in contrast to the generally "stable" orientations identified for single-crystal Ppv (Figure 7). In order to illustrate the effects of these unstable solutions, we applied a sensitivity cutoff to our textured Ppv simulations (Figure 8a, second row) to illustrate the effects of removing all

575 unstable solutions. If we consider only stable solutions, the probability of uniquely
576 constraining the starting orientation increases by 20% on average (Figure 9a).

577 In order to identify the starting orientation of the Ppv LPO, we found that a mixture
578 of SK(K)S and ScS shear wave splitting measurements again provide the highest likelihood
579 of constraining the orientation (Figure 8a: bottom, middle panel). There is a clear
580 dependence on angular dispersion (Figure 9a: bottom, right panel). Specifically, with low
581 values of R (0-0.1) and middle values of R (0.5-0.7), there is a higher probability of
582 constraining the orientation, while there is a decrease in probability between R = 0.1 and
583 R = 0.4. In all other cases and starting models, we have not observed this pattern of
584 dependence with R. While there is no explanation for this pattern, large values of R (0.8-
585 1.0) resulting in low probabilities of finding the starting orientation is consistent with all
586 other tests.

587 Returning to our consideration of single-crystal Ppv models, and as in section 3.2,
588 we considered the effect of adding a reflection measurement to shear wave splitting
589 observations to constrain the orientation of the single-crystal Ppv starting model (Figure
590 9b). For this test, we used a starting model that invokes an isotropic ppv layer over an
591 anisotropic ppv layer with dominant [100](010) slip (Model A in Figure 3). As in the
592 previous test, we find that just adding one observation of reflection polarity measurements
593 improves the probability of constraining the starting orientation (Figure 9b), although the
594 improvement was somewhat less dramatic. Again as with the previous tests, the relative
595 improvement is greatest for datasets with number of measurements N roughly between 5
596 and 9.

597 Finally, in a test analogous to the Gaussian noise test discussed in section 3.1 and
598 illustrated in Figure 7c, we considered a single-crystal Ppv test in which we tried to retrieve

599 the correct starting orientation using synthetic observations that included random, Gaussian
600 distributed errors on the fast polarization predictions (Figure 10). We found that adding
601 Gaussian noise to the fast polarization directions, normally distributed between -20° and
602 20° with a mean of 0° and standard deviation of 9°, does not significantly hinder the
603 probability of constraining the starting model's orientation (Figure 10a). However, this test
604 allowed us to explore the distinction between *uniquely* constraining the starting model's
605 orientation and identifying a model with a *minimum* misfit value that corresponds to the
606 correct starting orientation. For the error-free synthetic datasets, the minimum misfit value
607 always corresponds to the correct orientation, even for cases in which other orientations
608 are allowed by the data. For cases in which Gaussian error is incorporated to the synthetic
609 dataset; however, it is possible for the orientation with the minimum misfit value to be
610 different from the correct solution. This observation led us to carry out a test (Figure 10b)
611 in which rather than attempting to *uniquely* constrain the correct starting orientation, we
612 tested whether the best-fitting orientation (that is, the candidate orientation with the
613 minimum misfit value) actually corresponded to the correct starting orientation. We further
614 tested whether the best-fitting solution in terms of misfit was oriented within 10°-20° of
615 the known, correct starting orientation. Encouragingly, we found that the probability that
616 the minimum misfit solution was within 20° of the correct orientation exceeded 50% for
617 datasets with a relatively small number of shear wave splitting measurements ($N \approx 4$).
618
619 **4. Discussion**
620 4.1 Implications for the interpretation of real-world data sets
621 Understanding the scope of information about lowermost mantle anisotropy
622 contained in shear wave splitting and reflection polarity observations is crucial for our

623 ability to relate anisotropy observations to flow at the base of the mantle. While the
624 mechanisms of lowermost mantle anisotropy remain imperfectly known, the results
625 presented in this paper reveal observational strategies that can maximize the probability of
626 constraining the mechanism and/or orientation, regardless of the actual anisotropic
627 geometries present. This work shows that a diversity of shear wave splitting measurements
628 and reflection polarity data is essential, and the modeling of single phases (e.g., ScS, SKS,
629 SdS) is typically insufficient to constrain anisotropic geometry.

630 Specifically, this work demonstrates that because different seismic phases (ScS,
631 SKS, SKKS, PdP, SdS) propagate through or reflect off the D" region at different angles
632 from the horizontal, a combination of these phases is more useful for constraining
633 anisotropy than datasets with wide azimuthal coverage. Consider, for example, a
634 hypothetical case in which 9 unique splitting measurements for ScS phases are used to
635 probe an anisotropic structure consisting of horizontal, single crystal post-perovskite. In
636 this case, post-perovskite can only be distinguished from other plausible anisotropic
637 models less than 10% of the time (Figure 8a and 9a). However, if SK(K)S phases and/or
638 reflection polarities are incorporated into the analysis, then we can distinguish between the
639 two possible mechanisms nearly 40% of the time (Figure 8a). In all cases of varying starting
640 models and orientations, a combination of different types of data increases the probability
641 of constraining the starting model by 10% to 60%. This pattern also generally holds true
642 for finding the orientation of the Ppv elastic tensor. A diversity of data increases the
643 likelihood of constraining the orientation of Ppv anisotropy anywhere from 10% to 50%
644 for 6 unique measurements. Interestingly, we observed an exception to this (Figure 9a) for
645 Ppv oriented at an azimuth of 90°, where only ScS splitting data (SKS number of 0) had
646 the best chance to constrain the starting orientation.

Body wave datasets that probe seismic anisotropy in the lowermost mantle should combine both multiple data types and wide azimuthal coverage to maximize the probability that the anisotropic geometry can be tightly constrained. Figure 11 illustrates regions in the mantle in which all of the body wave measurement methods could potentially be applied simultaneously. This map was generated by considering the actual distribution of high-magnitude ($M > 6.5$) seismicity on Earth, in combination with a database of long-running broadband seismic stations beneath which the upper mantle anisotropy pattern has been shown to be simple enough to correct for (Lynner and Long, 2013, 2014b). While there are many regions of D" with limited raypath coverage for the types of data considered in this study, we find that North America, the Arctic, northwestern Pacific, and Australia are regions that represent ideal targets to collect a diverse set of observations to further constrain D" anisotropy.

Our results inform our view of why previous studies that included crossing raypaths (e.g., Ford et al., 2015; Creasy et al., 2017) were unable to uniquely constrain a model for D" anisotropy. Our study indicates that a relatively large number of shear wave splitting measurements (approximately 9 or more for most cases in Figure 8a) are needed to have at least a 40% to 60% chance of uniquely identifying the starting model. The observational datasets of Ford et al. (2015) and Creasy et al. (2017) included approximately four to eight shear wave splitting measurements over unique azimuths in the lowermost mantle (Table 3). The synthetic models presented in this paper help to provide context for why these studies have not been able to uniquely constrain a particular mechanism or orientation for anisotropy (e.g. Ford et al., 2015, Creasy et al., 2017). For example, each of these studies (Table 3) had relatively high angular dispersion values for their range of predicted fast splitting directions (greater than 0.4 in all cases). As discussed in section 3.2, datasets with

671 lower angular dispersion values are generally more successful at constraining a unique
672 elastic tensor. Therefore, even though many of the studies listed in Table 3 used diverse
673 data types with combinations of SKS, SKKS, and ScS, they could not uniquely constrain
674 an anisotropy mechanism or orientation when testing the elastic tensors considered in this
675 study. The studies that used one type of observation (Nowacki et al., 2010; Thomas et al.,
676 2011) did not consider all possible elastic tensors and orientations that we tested here, so
677 we cannot directly compare them with the results of our synthetic tests. If the mechanisms
678 for anisotropy and the associated elastic tensors can be reliably assumed, there is generally
679 a higher chance of identifying the correct orientation and inferring the correct mantle flow
680 geometry. With only 9 measurements, there is a 40% to 80% chance of uniquely
681 constraining the orientation of post-perovskite (Figure 9a), an improvement from the
682 chance of uniquely identifying the elastic tensor itself (a 40%-60% chance). Consideration
683 of these results in future studies of D" anisotropy, as well as a more detailed consideration
684 of how errors and uncertainties propagate in forward models, should enhance our ability to
685 characterize anisotropy at the base of the mantle. A more detailed statistical analysis may
686 be required similar to this study here to fully explore the error and model space.
687
688 4.2 Practical considerations
689 Our tests that assumed Gaussian error on the predicted fast splitting directions
690 (Figure 10b) demonstrate that it does not significantly affect the probability of constraining
691 the model, as compared to noise-free synthetic data. When including Gaussian error, we
692 found that as few as four shear wave splitting measurements can identify the correct
693 orientation within 20° more than 50% of the time. Datasets of this size (roughly four unique
694 measurements in the same region of D") can likely be reasonably achieved in many regions

of the lowermost mantle, based on the distribution of available raypaths (Figure 11). This finding may help with the interpretation of modeling results for real splitting datasets, such as those considered by Ford et al. (2015) and Creasy et al. (2017), for which multiple possible anisotropic orientations were identified, but particular orientations had significantly lower misfit values than others.

Our synthetic modeling results also shed light on potential complications in interpretation caused by the different symmetry classes of some of the candidate elasticity scenarios that have been proposed to explain lowermost mantle anisotropy. To effectively differentiate these scenarios using shear wave splitting data alone, it is crucial for splitting datasets to probe the symmetry of the mineral such that no other elastic tensor simulates that pattern for a similar range of propagation directions. Of the candidate scenarios we tested in this study, Fp has the highest (cubic) symmetry with only 3 unique constants in the elastic tensor. SPO models have the next highest symmetry, since tubule and oblate SPO models are hexagonal (transversely isotropic) with 5 unique elastic constants. Ppv and Br are both orthorhombic, with the same order of symmetry and only 9 unique elastic constants. In more complicated models, like LPO calculations of single crystals, the symmetry is much lower than its single crystal counterpart with 21 unique elastic constants.

4.3 Limitations of our modeling approach

We caution that our synthetic tests must be interpreted in light of the still-considerable limitations in our understanding of the elasticity of anisotropic materials at lowermost mantle conditions. We have focused mainly on single-crystal elastic tensors, derived mainly from ab initio simulations, as a reasonable starting point in this study; however, predictions of single-crystal elasticity are likely imperfect and do not take into

account effects such as variation in composition. Furthermore, single-crystal elasticity is an imperfect proxy for the likely anisotropic geometry of polycrystalline aggregates, particularly for minerals with high symmetry such as Fp (e.g., Yamazaki and Karato, 2002). The further consideration of elasticity models that explicitly take into account texture development will be an important step, although texture models include a number of poorly known parameters (such as activation energies for different slip systems) and consensus on the dominant slip systems in different lowermost mantle minerals remains elusive (e.g., Nowacki et al., 2011).

Another limitation of the work proposed here is that it is carried out in the context of ray theoretical predictions, assuming infinite frequency, rather than considering the full characteristics of the waveform at finite frequencies. With improvements on both observational and modeling techniques that model the full waveform (e.g., Kawai and Geller, 2010, Nowacki and Wookey, 2016, Parisi et al., 2018), the interpretation of seismic anisotropy observations can very likely be improved. In particular, future work must investigate how the measurement techniques used influence the interpretation of finite frequency waveform effects and to what extent ray theoretical predictions are a useful approximation. Despite these limitations, we expect that future work that predicts body wave observations in the presence of lowermost mantle anisotropy in a finite-frequency framework will likely find similar results: a diversity of seismic phases and measurement yields the best probability of capturing the symmetry, orientation, and properties of an elastic tensor. While this study is limited to a specific set of currently-available elastic tensors from the mineral physics literature, our overall findings should be generally applicable and adaptable to future improvements of our knowledge of lowermost mantle elasticity.

5. Summary

To summarize, the complete characterization and interpretation of seismic anisotropy at the base of the mantle would have profound effects on our understanding of lower mantle dynamics, potentially yielding insights into the pattern of mantle flow. Many recent studies have pointed to the difficulty of distinguishing different models of lowermost mantle anisotropy with body wave observations, given challenges with data coverage and uncertainties in the mechanism for anisotropy and the relationships between deformation and the resulting anisotropy at lower mantle conditions. In this study, we conducted a series of Monte Carlo simulations to determine what combination of body wave datasets (shear wave splitting and reflection polarities) are required to constrain D" anisotropy. We tested various starting models, orientations, and methods for the detection and identification of D” anisotropy. The modeling approach in this study is applicable to a wide range of elasticity models, and can be extended as our knowledge of the physical properties of the lowermost mantle increases. This approach can be used in future work on D” anisotropy to further explore how well a dataset can discriminate among possible elastic tensors.

Our results show that a diversity of observational techniques, including different types of seismic phases propagating over a range of raypath directions, are necessary in order to maximize the chances of constraining anisotropy at the base of the mantle. A combination of shear wave splitting measurements and observations of PdP and SdS reflection polarities in the same regions may be particularly powerful. We have further shown that if the mineralogy and/or mechanism for anisotropy can be constrained from independent data, then the orientation of the elastic tensor (and thus information about

766 patterns of mantle flow) can likely be retrieved from observational datasets that include a
767 relatively modest number of measurements.

Tables

Table 1

Summary of all elastic tensors used in the forward modeling. Columns show the type of tensor (single-crystal, LPO based on experimental data, SPO based on effective medium averaging, or LPO based on global flow and texture models), the phases and/or constituents, and the reference. For the single-crystal tensors, the pressure and temperature conditions used in the modeling are also indicated. [1]Elastic tensors used for tests to uniquely constrain the starting model. [2]Elastic tensors used for tests to uniquely constrain the orientation.

Single Crystal Tensors				
Geometry	Phase	Pressure (GPa)	Temperature (K)	References
Single Crystal	Br[1]	125 126 136	2500 2800 4000	*Wentzcovitch et al.* [2006], *Wookey et al.* [2005a, 2005b]
	Ppv[1,2]	135	4000	*Stackhouse et al.* [2005]
	MgO[1]	135	3000	*Karki et al.* [1999]
Other Tensors				
Geometry	Phase	Notes		References
Experimental LPO	MgO[1]	P = 0.3 GPa; T = 1473K		*Long et al.* [2006]
SPO[1]	0.003 vol. fraction melt	Oblate shape		*Walker and Wookey* [2012]
	0.003 vol. fraction melt	Tubule shape		*Walker and Wookey* [2012]
Calculated LPO[2]	Ppv	TX2008-V1 model; dominant slip plane: (010), P = 125-136; T = 3000-4000 K		*Walker et al.* [2011]; Tensors based on *Stackhouse et al.,* [2005] and *Stackhouse and Brodholt* [2007]

Table 2

781 Models for the top (isotropic) and bottom (anisotropic) layers of each model described in
782 Figure 3 for reflection polarity models. The dominant slip system assumed in each bottom
783 layer is listed.

Model	Top Layer (isotropic)	Bottom Layer (anisotropic)	Slip System	References
A	Ppv	Ppv	[100](010)	*Walte et al. [2009]* *Wentzcovitch et al. [2006]*
B	Br	Ppv	[100](010)	*Walte et al. [2009]* *Wentzcovitch et al. [2006]*
C	Br	Br	[010](100)	*Stackhouse et al. [2005]* *Mainprice et al. [2008]*
D	Fp	Fp	[100](001)	*Karki et al. [1999]*

784

785

786 Table 3

787 Summary of previous studies that have used crossing raypaths to study D" anisotropy, as
788 identified in Figure 1. The number of unique azimuths is given; each azimuth typically
789 contains multiple observations (in practice, these observations are typically averaged for
790 each set of raypaths). SKS number is calculated as defined in the text; for example,
791 Nowacki et al. (2010) used only ScS phases, therefore the SKS number is 0. Angular
792 dispersion (R) of the raypath azimuths is also calculated as described in the text.

References	Region	Number of Unique Azimuths	SKS Number	R
Creasy et al., 2017	New Zealand	8	0.75	0.7866
Creasy et al., 2017	SW Australia	4	0.5	0.4297
Ford et al., 2015	Afar Peninsula	5	0.6	0.8305
Thomas et al., 2011	Siberia + Caribbean	4	reflection polarities	0.5801
Nowacki et al., 2010	Caribbean	6	0	0.5734

793

794 **Figure Captions**

795 Figure 1. Summary map of previously published studies (which include shear wave
796 splitting measurements and reflection polarity observations) to constrain D" anisotropy,
797 updated and adapted from Nowacki et al. (2011). Highlighted areas (pink/gray) indicate
798 regions that have been probed for D" anisotropy with these methods. Regions in pink
799 indicate studies that used multiple techniques and/or intersecting ray paths, for which at
800 least two observations intersect in the same region with different propagation azimuths.
801 Two such studies are highlighted on the right. Panel (a) shows the raypaths (black lines)
802 beneath Siberia studied in the reflection polarity study of Thomas et al. (2011). CMB
803 bounce points are indicated with diamonds and circles, and the dotted arrow indicates paleo
804 subduction direction 100 Ma ago of the Kula plate. Background colors indicate P wave
805 velocity deviations at the base of the mantle from the model of Kárason and Hilst (2001).
806 Panel (b) shows a schematic diagram of shear wave splitting measurements of SKS (green),
807 SKKS (red) , and ScS (blue) phases beneath the Afar region of Africa (Ford et al., 2015).
808 Background colors show S wave velocity deviations at a depth of 250 km above core
809 mantle boundary from the GyPSuM tomography model (Simmons et al., 2010).
810
811 Figure 2. Elastic properties of models from Table 1 for D" anisotropy tested in this
812 study, as expressed in the predicted shear wave splitting behavior. Predicted shear wave
813 splitting behavior is shown as a 3D spherical representation relative to geographic space,
814 with the [100], [010], and [001] axes indicated in order to view the variation of splitting of
815 SKS, SKKS, and ScS with azimuth. The anisotropy 3-D spheres show the directional
816 dependence of seismic anisotropy (strength [gray color bar] and fast-axis directions [black
817 bars]). For each model, the [100] and [010] axes are parallel to the CMB and oriented north

and west, respectively. Black bars show predicted splitting over a range inclinations and azimuths, as computed using the MSAT toolkit (Walker and Wookey, 2012). Magenta bars illustrate the predicted fast polarization directions for the given starting models for a particular set of SKS, SKKS, and ScS raypaths every 20° (we actually use steps of 5° in the synthetic modeling, but the plotting is too dense to show) that are evenly distributed. Inclination angles used in the modeling are based on the average inclination angles for each phase through the D" layer; we assume that ScS propagates nearly horizontally through the lowermost mantle, as described in the text. From left to right, we show elastic tensor models for single-crystal Ppv (Stackhouse et al., 2005), single-crystal Br (Wentzcovitch et al., 2006), single-crystal Fp (Karki et al., 1999: Labeled as "Fp (Karki)"), experimentally-derived LPO of Fp (Long et al., 2006: Labeled as “Fp (Long)”), Oblate SPO (Walker and Wookey, 2012), Tubule SPO (Walker and Wookey, 2012), and the averaged, textured Ppv (Walker et al., 2011). Background colors are %S-wave anisotropy.

Figure 3. Predictions of reflection polarities for PdP and SdS waves for different D" anisotropy models shown as an upper hemispherical projection since polarities depend on azimuth, not inclination as in Figure 2. Predictions are made as a function of azimuth and epicentral distance (from 60° to 80°). Azimuth is relative to the slip direction (indicated by the black arrow), which also corresponds to direction of lowermost mantle flow for a simple horizontal shear geometry. The first two columns show the reflection coefficients of P-P and SH-SH upon reflection off the D" discontinuity, located 300 km above the core mantle boundary in the model. Blue and red regions indicate positive and negative polarities, respectively. Models A, C, and D illustrate situations where there is an onset of anisotropy at the D" discontinuity while Model B invokes both a phase change (from Br to

842 Ppv) and the onset of anisotropy. The last column illustrates the predicted S wave
843 anisotropy (color bar) and predicted shear wave splitting fast directions (black bars) for the
844 same models, plotted as a function of azimuth and inclination from the horizontal. Elastic
845 tensors corresponding to these models are shown in Table 2.
846
847 Figure 4. Flow chart of steps in our modeling framework. The first step is to identify
848 the starting model and its orientation from Tables 1 or 2. Secondly, randomly choose an
849 azimuthal distribution of raypaths through the starting model and fix the SKS number.
850 Thirdly, use the raypaths from step 2 and calculate the fast polarization directions and/or
851 reflection polarities (splitting parameters) based on the identified starting model and SKS
852 number. Fourth, use this synthetic dataset to use the forward modeling approach to identify
853 which models and orientations fit the synthetic dataset. We apply the misfit cutoff as
854 described in Methods to eliminate certain models and orientations in order to see if the
855 synthetic dataset can uniquely constrain the starting model. Lastly, in step 5, we repeat this
856 same process M times (number of iterations), identifying a new random distribution of
857 raypaths each time.
858
859 Figure 5. An illustrative example of how shear wave splitting predictions for an
860 individual iteration in our stochastic modeling scheme are calculated. (a) Plane view
861 (looking down from above on CMB) of starting model for Ppv (Stackhouse et al., 2005)
862 showing S wave % anisotropy (colors), with fast polarization directions plotted as black
863 bars. (b) Raypath distribution for this example for SKS (red), SKKS (orange), and ScS
864 (blue), plotted as azimuth from north. (c) The predicted fast polarization directions based
865 on the starting model in (a) and the raypath distribution in (b). Colors indicate phase type.

Figure 6. Results of a test of how many iterations are needed for the model results to converge. The x-axis defines the number of iterations (M) (that is, number of unique raypath configurations with similar characteristics) that were successively carried out. The y-axis indicates what percentage of the iterations run could be uniquely constrained. This particular test used 9 shear wave splitting measurements and a starting model of horizontal Ppv, and we found that after a large number of iterations, the starting model could be constrained for 41% of all iterations carried out. In contrast, for the other 59%, a unique solution of Ppv could not be constrained for that particular synthetic dataset. Based on the results of this test, at least 5,000 iterations were carried out for each test described in this study.

Figure 7. An example of how the forward modeling method identifies all possible orientations of the Ppv single crystal elastic tensor that fit a particular synthetic dataset. We show two synthetic datasets of 8 (a) and 4 (b) unique synthetic measurements with 3 SKS, 3 SKKS, 2 ScS measurements and 1 SKS, 2 SKKS, and 1 ScS measurements, respectively. The last case (c) shows a test with the same 4 synthetic measurements as in (b) but with Gaussian distributed random error to the predicted fast directions. These projections show all possible permissible orientations (colored dots) of the Ppv tensor for the given synthetic dataset plotted as an upper hemispherical projection of the [100], [010], and [001] axes. The white dots mark local minima, where the magenta dots represent the global minimum. The magenta dots indicate the global minimum misfit, which should be equal to a non-rotated Ppv (that is, horizontal [100] and [010] axes and vertical [001] axis).

890 Figure 8: Results of synthetic tests that aim to uniquely constrain the starting
891 model/mechanism, as discussed in section 3.2. Three different sets of tensors were tested,
892 while three different aspects of the raypath configuration were varied. In (a), each row
893 shows plots of the probability of uniquely identifying the given starting model (Ppv, Br,
894 and MgO). Each column represents the variable describing raypath configuration that was
895 allowed to vary, while the other two were fixed. In the first column, we varied the number
896 of measurements N, but fixed the SKS ratio (0.67) and tested the full range of possible R
897 values. In the second column, we varied SKS number but fixed the number of
898 measurements (N = 9) and tested the full range of possible R values. In the third column,
899 we varied the angular dispersion R, but fixed the number of measurements and SKS
900 number (N = 9 and SKS = 0.6). We further tested a range of starting orientations for each
901 starting model (three for Ppv and Br, two for Fp); the labels (0, 45, 90) refer to the rotation
902 angle (in degrees) about the [100] axis from the horizontal. In (b), we chose Model A in
903 Figure 3 as the starting model and tested whether we could uniquely constrain this starting
904 model using a combination of shear wave splitting and reflection measurements. For this
905 test, the SKS number was fixed (0.67) and we tested the full range of possible angular
906 dispersion values. The test shown in (b: left image) compares synthetic datasets with only
907 shear wave splitting measurements (black line, SS) to those that include splitting plus one
908 additional reflection measurement for a P and S reflected phase off the D" over a randomly
909 defined azimuth (gray line, SS+R). The difference in probability between these two raypath
910 configuration scenarios is shown in right image.
911
912 Figure 9. Results of synthetic tests that aim to uniquely constrain the orientation of
913 a Ppv starting model, as discussed in section 3.3. In (a), each row shows plots of the

914 probability of uniquely identifying the given starting model's orientation using the
915 synthetic data, for three different orientations about the [100] axis in the starting model, as
916 shown in the legend (with the labels 0 and 90, referring to the angle about the [100] axis)
917 and described in the text. As in Figure 7, each column represents the variable that was
918 allowed to vary, while the other two were fixed. The second row illustrates the results of
919 tests that aimed to uniquely constraining the starting model orientation for textured Ppv
920 models invoking slip on the (010) plane (Walker et al., 2011). For these tests, we
921 distinguish between scenarios in which we increased the sensitivity (that is, discarded
922 "unstable" solutions, as described in the text). Tests in which unstable solutions were
923 discarded (gray line) increased the probability of identifying the orientation of anisotropy
924 in comparison to retaining unstable solutions (black line). In (b), we show results of tests
925 of the effect of adding one additional reflection measurement to the shear wave splitting
926 measurements, using Model A in Figure 3 as the starting model. For these tests, the SKS
927 number was fixed (0.67) and we tested the full range of possible angular dispersion values.
928 The test shown in (b: left image) compares synthetic datasets with only shear wave splitting
929 measurements (black line, SS) to those that include splitting plus one additional reflection
930 measurement for a P and S reflected phase off the D" over a randomly defined azimuth
931 (gray line, SS+R). The difference in probability between these two raypath configuration
932 scenarios is shown at right.
933
934 Figure 10: Results of tests that aimed to uniquely identify the orientation of a single-
935 crystal Ppv starting model, with Gaussian distributed random errors (standard deviation =
936 9°) incorporated into the synthetic shear wave splitting dataset. In (a), we varied the number
937 of shear wave splitting measurements and calculated the probabilities of correctly

retrieving the starting model orientation. In (b), we plot the probability of correctly identifying the starting orientation for a synthetic dataset with Gaussian error applied based on an identification of the minimum misfit (as opposed to searching for a unique solution). In (b), the black line (unique solution, same as in (a)) shows the probability of uniquely constraining the orientation of the starting model. The other two lines show the probability of identifying the correct solution within 10° or 20° by using the minimum misfit.

Figure 11. Map of regions of the lowermost mantle in which the various measurement methods (SKS [distance range: 108° – 122°], SKKS [108° – 122°], and ScS [60° – 80°] shear wave splitting and reflection polarities) used in this study could potentially be applied. We parameterize the D" layer into a 5° by 5° grid. We calculated raypaths for different seismic phases using TauP (Crotwell et al., 1999) assuming a 250km thick D" layer. We used a set of seismic stations with simple upper mantle anisotropy (Lynner and Long, 2013, 2014b) for all events greater than Mw6.5 that occurred in the time span of deployment for each seismic station for SKS, SKKS, and ScS. For reflection polarities, we considered only dense arrays openly available: TAMNNET, POLENET, GAMSEIS, Yellowknife Array, KNET, Southern California Network, GRSN Array, F-Net, USArray (using stations in Alaska), USArray (using stations in Texas), USArray (using stations in Minnesota), USArray (using stations in New York), USArray (using stations in South Carolina), and the Pacific Northwest Seismic Network.

Acknowledgements

This work was supported by a National Science Foundation (NSF) Graduate Research Fellowship grant DGE-1122492 to N.C. and by NSF grant EAR-1547499 to M.D.L. Some

figures were prepared using the Generic Mapping Tools (Wessel and Smith, 1991). We thank the Yale Center for Research Computing for guidance and use of the research computing infrastructure, specifically Kaylea Nelson. AP received funding from the European Union's Horizon 2020 research and innovation program under the Marie Sklodowska-Curie grant agreement No 642029 - ITN CREEP. We are grateful to Sanne Cottaar, Jeroen Ritsema, and editor Ana Ferreira for thoughtful and constructive comments that helped us to improve the paper.

971 **References**

972

973 Bendat, J.S., Piersol, A.G., 2011. Random Data: Analysis and Measurement Procedures.
974 John Wiley & Sons.
975 Cottaar, S., Romanowicz, B., 2013. Observations of changing anisotropy across the
976 southern margin of the African LLSVP. Geophys. J. Int. ggt285.
977 https://doi.org/10.1093/gji/ggt285
978 Creasy, N., Long, M.D., Ford, H.A., 2017. Deformation in the lowermost mantle beneath
979 Australia from observations and models of seismic anisotropy. J. Geophys. Res.
980 Solid Earth 122, 2016JB013901. https://doi.org/10.1002/2016JB013901
981 Crotwell, H.P., Owens, T.J., Ritsema, J., 1999. The TauP Toolkit: Flexible Seismic
982 Travel-time and Ray-path Utilities. Seismol. Res. Lett. 70, 154–160.
983 https://doi.org/10.1785/gssrl.70.2.154
984 Deng, J., Long, M.D., Creasy, N., Wagner, L., Beck, S., Zandt, G., Tavera, H., Minaya,
985 E., 2017. Lowermost mantle anisotropy near the eastern edge of the Pacific
986 LLSVP: constraints from SKS–SKKS splitting intensity measurements. Geophys.
987 J. Int. 210, 774–786. https://doi.org/10.1093/gji/ggx190
988 Ford, H.A., Long, M.D., 2015. A regional test of global models for flow, rheology, and
989 seismic anisotropy at the base of the mantle. Phys. Earth Planet. Inter. 245, 71–75.
990 https://doi.org/10.1016/j.pepi.2015.05.004
991 Ford, H.A., Long, M.D., He, X., Lynner, C., 2015. Lowermost mantle flow at the eastern
992 edge of the African Large Low Shear Velocity Province. Earth Planet. Sci. Lett.
993 420, 12–22. https://doi.org/10.1016/j.epsl.2015.03.029
994 Ford R., Garnero Edward J., McNamara Allen K., 2006. A strong lateral shear velocity
995 gradient and anisotropy heterogeneity in the lowermost mantle beneath the
996 southern Pacific. J. Geophys. Res. Solid Earth 111.
997 https://doi.org/10.1029/2004JB003574
998 Garnero, E.J., McNamara, A.K., Shim, S.-H., 2016. Continent-sized anomalous zones
999 with low seismic velocity at the base of Earth's mantle. Nat. Geosci. 9, 481–489.
1000 https://doi.org/10.1038/ngeo2733
1001 Goryaeva, A.M., Carrez, P., Cordier, P., 2017. Modeling defects and plasticity in
1002 MgSiO<Subscript>3</Subscript> post-perovskite: Part 3—Screw and edge [001]
1003 dislocations. Phys. Chem. Miner. 44, 521–533. https://doi.org/10.1007/s00269-
1004 017-0879-0
1005 Groos, J.C., Ritter, J.R.R., 2009. Time domain classification and quantification of seismic
1006 noise in an urban environment. Geophys. J. Int. 179, 1213–1231.
1007 https://doi.org/10.1111/j.1365-246X.2009.04343.x
1008 Guest, W.S., Kendall, J.M., 1993. Modeling seismic waveforms in anisotropic media
1009 using maslov asymptotic theory. J. Explor. Geophys. 29, 78–92.
1010 Kárason, H., Hilst, R.D. van der, 2001. Tomographic imaging of the lowermost mantle
1011 with differential times of refracted and diffracted core phases (PKP, Pdiff). J.
1012 Geophys. Res. Solid Earth 106, 6569–6587.
1013 https://doi.org/10.1029/2000JB900380
1014 Karki, B.B., Wentzcovitch, R.M., Gironcoli, S. de, Baroni, S., 1999. First-Principles
1015 Determination of Elastic Anisotropy and Wave Velocities of MgO at Lower

Mantle Conditions. Science 286, 1705–1707. https://doi.org/10.1126/science.286.5445.1705

Kawai, K., Geller, R.J., 2010. The vertical flow in the lowermost mantle beneath the Pacific from inversion of seismic waveforms for anisotropic structure. Earth Planet. Sci. Lett. 297, 190–198. https://doi.org/10.1016/j.epsl.2010.05.037

Kendall, J.-M., Silver, P.G., 1998. Investigating Causes of D″ Anistropy, in: The Core-Mantle Boundary Region. American Geophysical Union, Washington D.C., pp. 409–412.

Lay T., Helmberger D.V., 1983. The shear-wave velocity gradient at the base of the mantle. J. Geophys. Res. Solid Earth 88, 8160–8170. https://doi.org/10.1029/JB088iB10p08160

Lee, K.K.M., O'Neill, B., Panero, W.R., Shim, S.-H., Benedetti, L.R., Jeanloz, R., 2004. Equations of state of the high-pressure phases of a natural peridotite and implications for the Earth's lower mantle. Earth Planet. Sci. Lett. 223, 381–393. https://doi.org/10.1016/j.epsl.2004.04.033

Long Maureen D., Lynner Colton, 2015. Seismic anisotropy in the lowermost mantle near the Perm Anomaly. Geophys. Res. Lett. 42, 7073–7080. https://doi.org/10.1002/2015GL065506

Long, M.D., 2009. Complex anisotropy in D″ beneath the eastern Pacific from SKS–SKKS splitting discrepancies. Earth Planet. Sci. Lett. 283, 181–189. https://doi.org/10.1016/j.epsl.2009.04.019

Long, M.D., Xiao, X., Jiang, Z., Evans, B., Karato, S., 2006. Lattice preferred orientation in deformed polycrystalline (Mg,Fe)O and implications for seismic anisotropy in D″. Phys. Earth Planet. Inter. 156, 75–88. https://doi.org/10.1016/j.pepi.2006.02.006

Lynner, C., Long, M.D., 2014a. Lowermost mantle anisotropy and deformation along the boundary of the African LLSVP. Geophys. Res. Lett. 41, 2014GL059875. https://doi.org/10.1002/2014GL059875

Lynner, C., Long, M.D., 2014b. Sub-slab anisotropy beneath the Sumatra and circum-Pacific subduction zones from source-side shear wave splitting observations. Geochem. Geophys. Geosystems 15, 2262–2281. https://doi.org/10.1002/2014GC005239

Lynner, C., Long, M.D., 2013. Sub-slab seismic anisotropy and mantle flow beneath the Caribbean and Scotia subduction zones: Effects of slab morphology and kinematics. Earth Planet. Sci. Lett. 361, 367–378. https://doi.org/10.1016/j.epsl.2012.11.007

Mardia, K.V., Jupp, P.E., 2000. Directional statistics. Wiley.

McNamara, A.K., Karato, S.-I., van Keken, P.E., 2001. Localization of dislocation creep in the lower mantle: implications for the origin of seismic anisotropy. Earth Planet. Sci. Lett. 191, 85–99. https://doi.org/10.1016/S0012-821X(01)00405-8

Meade, C., Silver, P.G., Kaneshima, S., 1995. Laboratory and seismological observations of lower mantle isotropy. Geophys. Res. Lett. 22, 1293–1296. https://doi.org/10.1029/95GL01091

Mitrovica, J.X., Forte, A.M., 2004. A new inference of mantle viscosity based upon joint inversion of convection and glacial isostatic adjustment data. Earth Planet. Sci. Lett. 225, 177–189. https://doi.org/10.1016/j.epsl.2004.06.005

Murakami, M., Hirose, K., Kawamura, K., Sata, N., Ohishi, Y., 2004. Post-Perovskite Phase Transition in MgSiO3. Science 304, 855–858. https://doi.org/10.1126/science.1095932

Nowacki, A., Wookey, J., 2016. The limits of ray theory when measuring shear wave splitting in the lowermost mantle with ScS waves. Geophys. J. Int. 207, 1573–1583. https://doi.org/10.1093/gji/ggw358

Nowacki, A., Wookey, J., Kendall, J.-M., 2011. New advances in using seismic anisotropy, mineral physics and geodynamics to understand deformation in the lowermost mantle. J. Geodyn. 52, 205–228. https://doi.org/10.1016/j.jog.2011.04.003

Nowacki, A., Wookey, J., Kendall, J.-M., 2010. Deformation of the lowermost mantle from seismic anisotropy. Nature 467, 1091–1094. https://doi.org/10.1038/nature09507

Parisi, L., Ferreira, A.M.G., Ritsema, J., 2018. Apparent Splitting of S Waves Propagating Through an Isotropic Lowermost Mantle. J. Geophys. Res. Solid Earth 123. https://doi.org/10.1002/2017JB014394

Simmons, N.A., Forte, A.M., Boschi, L., Grand, S.P., 2010. GyPSuM: A joint tomographic model of mantle density and seismic wave speeds. J. Geophys. Res. Solid Earth 115, B12310. https://doi.org/10.1029/2010JB007631

Simmons, N.A., Forte, A.M., Grand, S.P., 2009. Joint seismic, geodynamic and mineral physical constraints on three-dimensional mantle heterogeneity: Implications for the relative importance of thermal versus compositional heterogeneity. Geophys. J. Int. 177, 1284–1304. https://doi.org/10.1111/j.1365-246X.2009.04133.x

Simmons, N.A., Myers, S.C., Johannesson, G., Matzel, E., Grand, S.P., 2015. Evidence for long-lived subduction of an ancient tectonic plate beneath the southern Indian Ocean. Geophys. Res. Lett. 42, 2015GL066237. https://doi.org/10.1002/2015GL066237

Stackhouse, S., Brodholt, J.P., Wookey, J., Kendall, J.-M., Price, G.D., 2005. The effect of temperature on the seismic anisotropy of the perovskite and post-perovskite polymorphs of MgSiO3. Earth Planet. Sci. Lett. 230, 1–10. https://doi.org/10.1016/j.epsl.2004.11.021

Thomas, C., Wookey, J., Brodholt, J., Fieseler, T., 2011a. Anisotropy as cause for polarity reversals of D″ reflections. Earth Planet. Sci. Lett. 307, 369–376. https://doi.org/10.1016/j.epsl.2011.05.011

Thomas, C., Wookey, J., Simpson M., 2007. D″ anisotropy beneath Southeast Asia. Geophys. Res. Lett. 34. https://doi.org/10.1029/2006GL028965

Walker, A.M., Forte, A.M., Wookey, J., Nowacki, A., Kendall, J.-M., 2011. Elastic anisotropy of D″ predicted from global models of mantle flow. Geochem. Geophys. Geosystems 12, Q10006. https://doi.org/10.1029/2011GC003732

Walker, A.M., Wookey, J., 2012. MSAT—A new toolkit for the analysis of elastic and seismic anisotropy. Comput. Geosci. 49, 81–90. https://doi.org/10.1016/j.cageo.2012.05.031

Walte, N.P., Heidelbach, F., Miyajima, N., Frost, D.J., Rubie, D.C., Dobson, D.P., 2009. Transformation textures in post-perovskite: Understanding mantle flow in the D″ layer of the Earth. Geophys. Res. Lett. 36, L04302. https://doi.org/10.1029/2008GL036840

Wang, Y., Wen, L., 2007. Geometry and P and S velocity structure of the "African Anomaly." J. Geophys. Res. Solid Earth 112, B05313. https://doi.org/10.1029/2006JB004483

Wentzcovitch, R.M., Tsuchiya, T., Tsuchiya, J., 2006. MgSiO3 postperovskite at D″ conditions. Proc. Natl. Acad. Sci. U. S. A. 103, 543–546. https://doi.org/10.1073/pnas.0506879103

Wookey, J., Kendall, J.-M., 2008. Constraints on lowermost mantle mineralogy and fabric beneath Siberia from seismic anisotropy. Earth Planet. Sci. Lett. 275, 32–42. https://doi.org/10.1016/j.epsl.2008.07.049

Wookey, J., Kendall, J.-M., Rümpker, G., 2005a. Lowermost mantle anisotropy beneath the north Pacific from differential S—ScS splitting. Geophys. J. Int. 161, 829–838. https://doi.org/10.1111/j.1365-246X.2005.02623.x

Wookey, J., Stackhouse, S., Kendall, J.-M., Brodholt, J., Price, G.D., 2005b. Efficacy of the post-perovskite phase as an explanation for lowermost-mantle seismic properties. Nature 438, 1004–1007. https://doi.org/10.1038/nature04345

Yamazaki, D., Yoshino, T., Ohfuji, H., Ando, J., Yoneda, A., 2006. Origin of seismic anisotropy in the D″ layer inferred from shear deformation experiments on post-perovskite phase. Earth Planet. Sci. Lett. 252, 372–378. https://doi.org/10.1016/j.epsl.2006.10.004

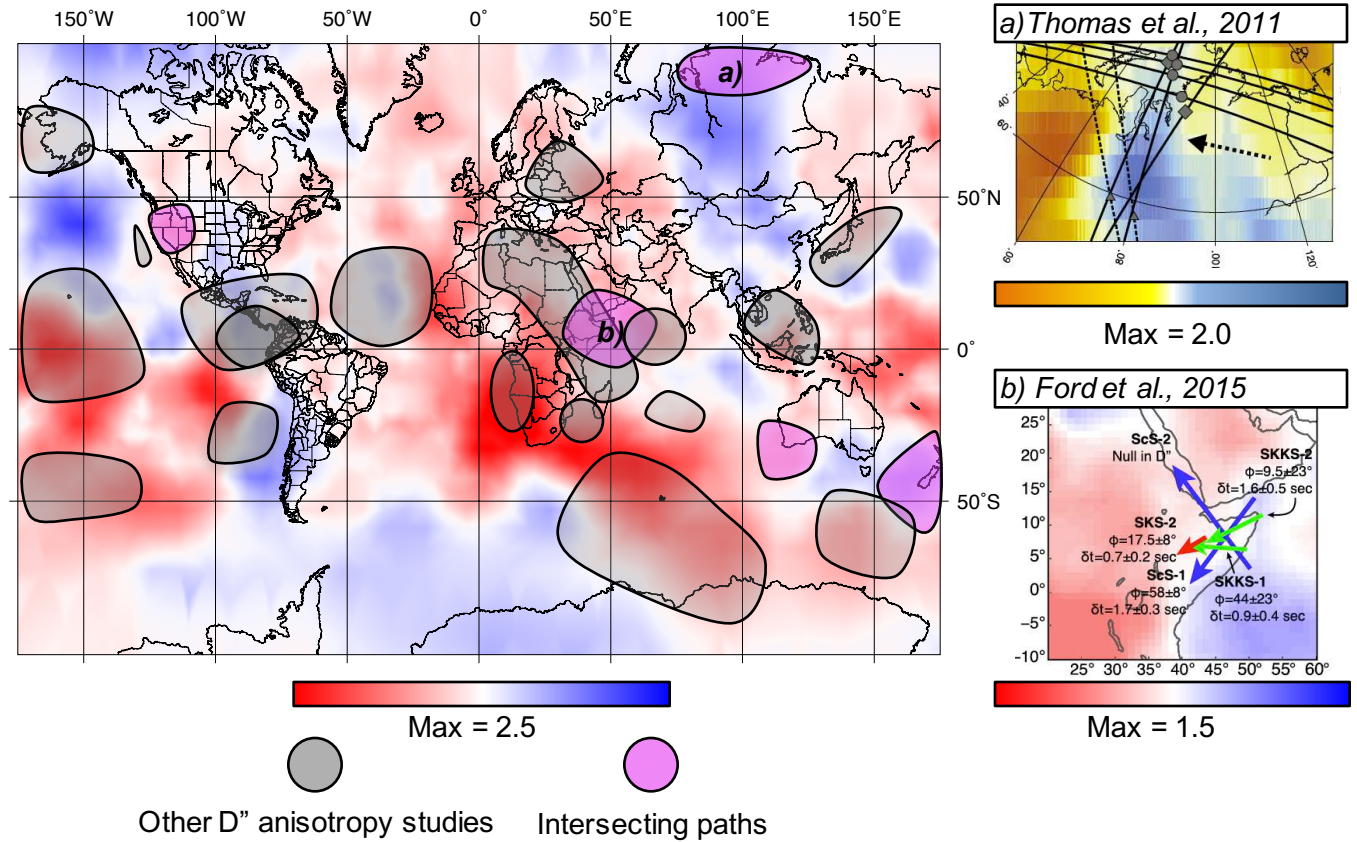
150˚W
100˚W
50˚W
0˚
50˚E
100˚E
150˚E
50˚N
0˚
50˚S
a)
b)
Max = 2.5
Other D” anisotropy studies
Intersecting paths
a) Thomas et al., 2011
Max = 2.0
b) Ford et al., 2015
ScS-2
Null in D”
SKKS-2
ϕ=9.5±23°
δt=1.6±0.5 sec
SKS-2
ϕ=17.5±8°
δt=0.7±0.2 sec
ScS-1
ϕ=58±8°
δt=1.7±0.3 sec
SKKS-1
ϕ=44±23°
δt=0.9±0.4 sec
Max = 1.5

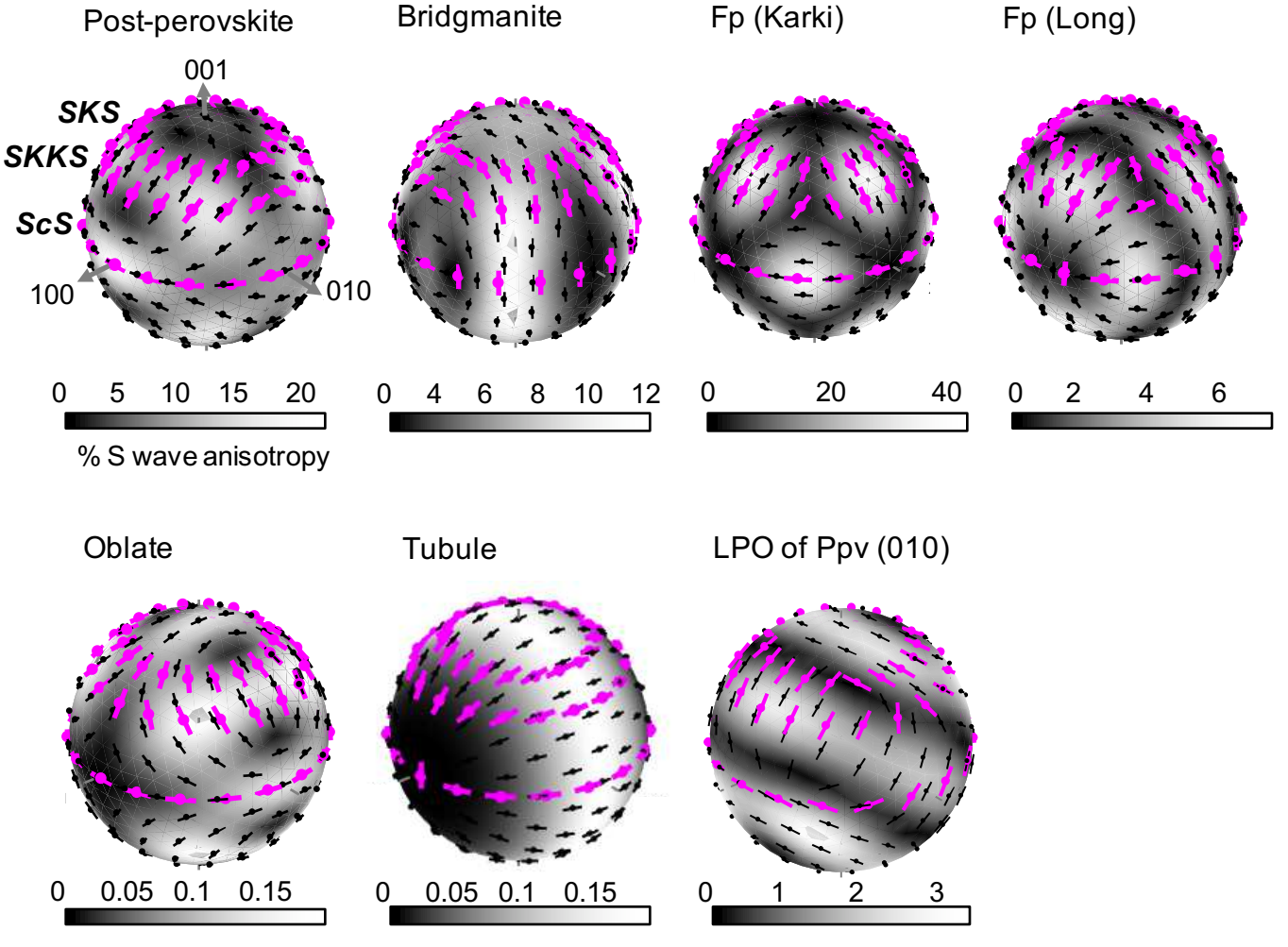
Post-perovskite
001
SKS
SKKS
ScS
100
010
0 5 10 15 20
% S wave anisotropy
Bridgmanite
0 4 6 8 10 12
Fp (Karki)
0 20 40
Fp (Long)
0 2 4 6
Oblate
0 0.05 0.1 0.15
Tubule
0 0.05 0.1 0.15
LPO of Ppv (010)
0 1 2 3

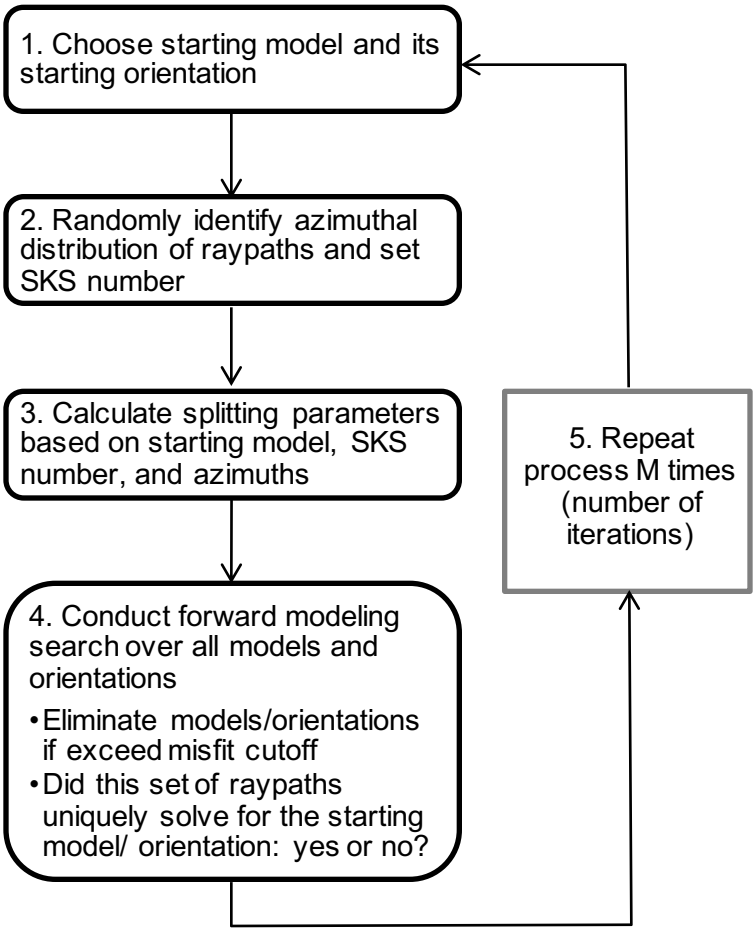
1. Choose starting model and its starting orientation
2. Randomly identify azimuthal distribution of raypaths and set SKS number
3. Calculate splitting parameters based on starting model, SKS number, and azimuths
4. Conduct forward modeling search over all models and orientations
• Eliminate models/orientations if exceed misfit cutoff
• Did this set of raypaths uniquely solve for the starting model/ orientation: yes or no?
5. Repeat process M times (number of iterations)

a) Starting Model

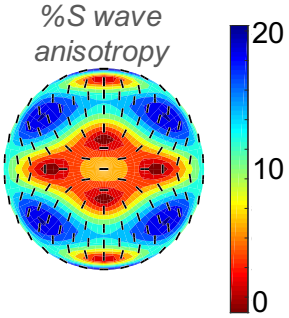

b) Select Number of Observations and their Azimuths

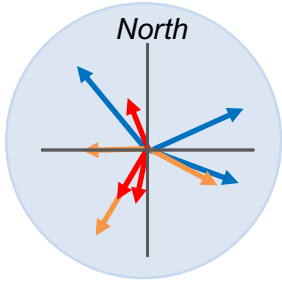

9 shear wave splitting measurements

- 3 *SKS*
- 3 *SKKS*
- 3 *ScS*

c) Calculate Fast Polarization Directions

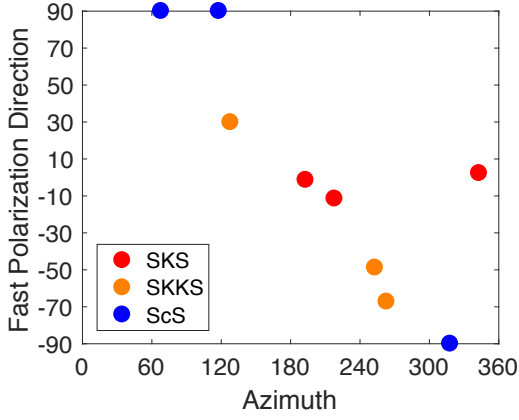

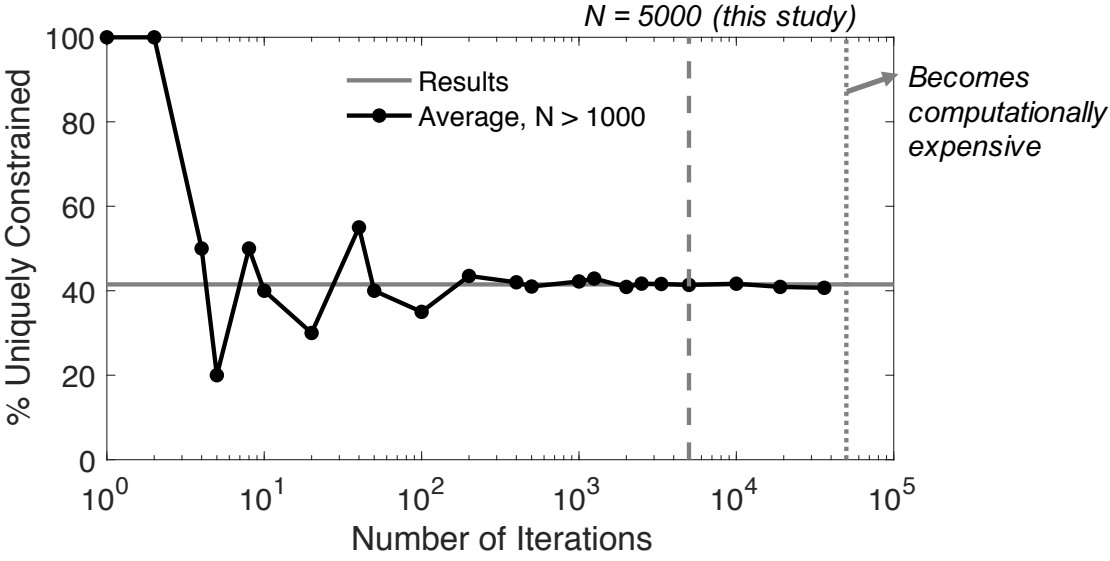
N = 5000 (this study)
Results
Average, N > 1000
Becomes computationally expensive
% Uniquely Constrained
Number of Iterations
100
80
60
40
20
0
10^0
10^1
10^2
10^3
10^4
10^5

(a) 8 Measurements

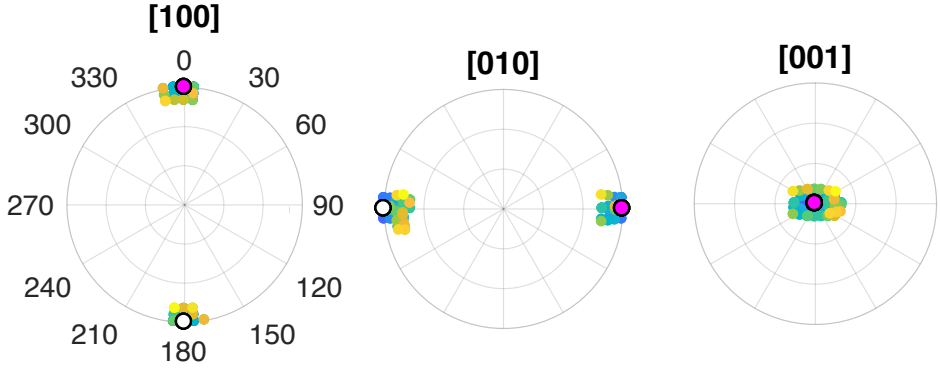

(b) 4 Measurements

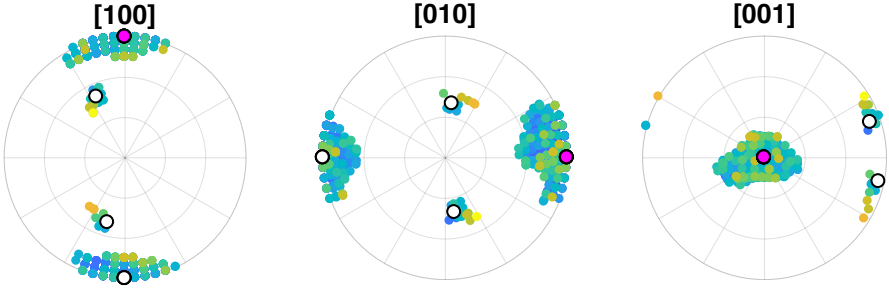

(c) 4 Measurements with Gaussian Error

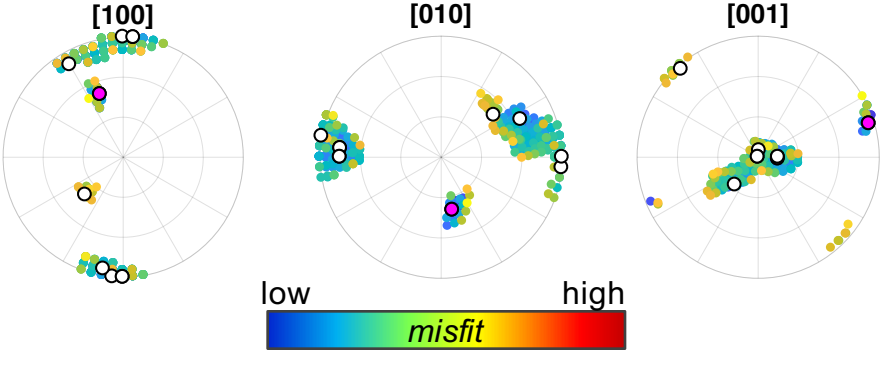

(a) Changes in the Starting Model

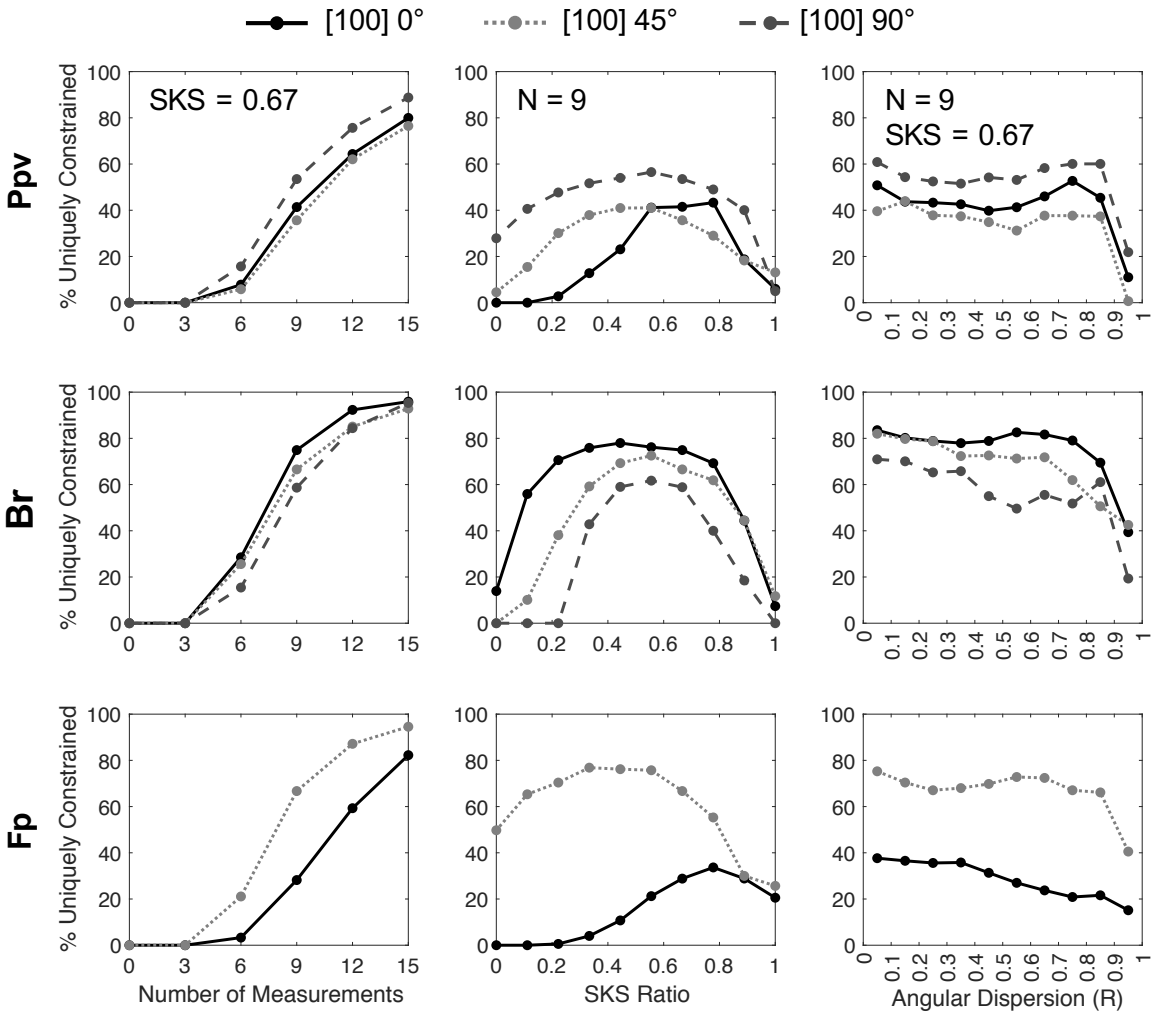

(b) Adding 1 Reflection Measurement

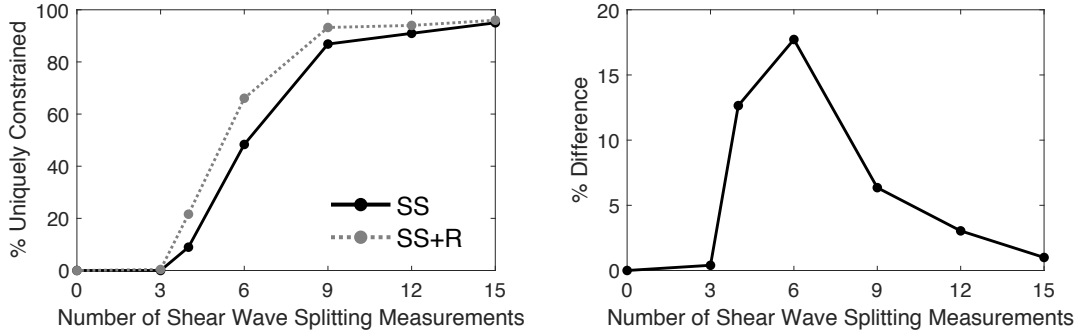

(a) Changes in the Starting Model Orientation

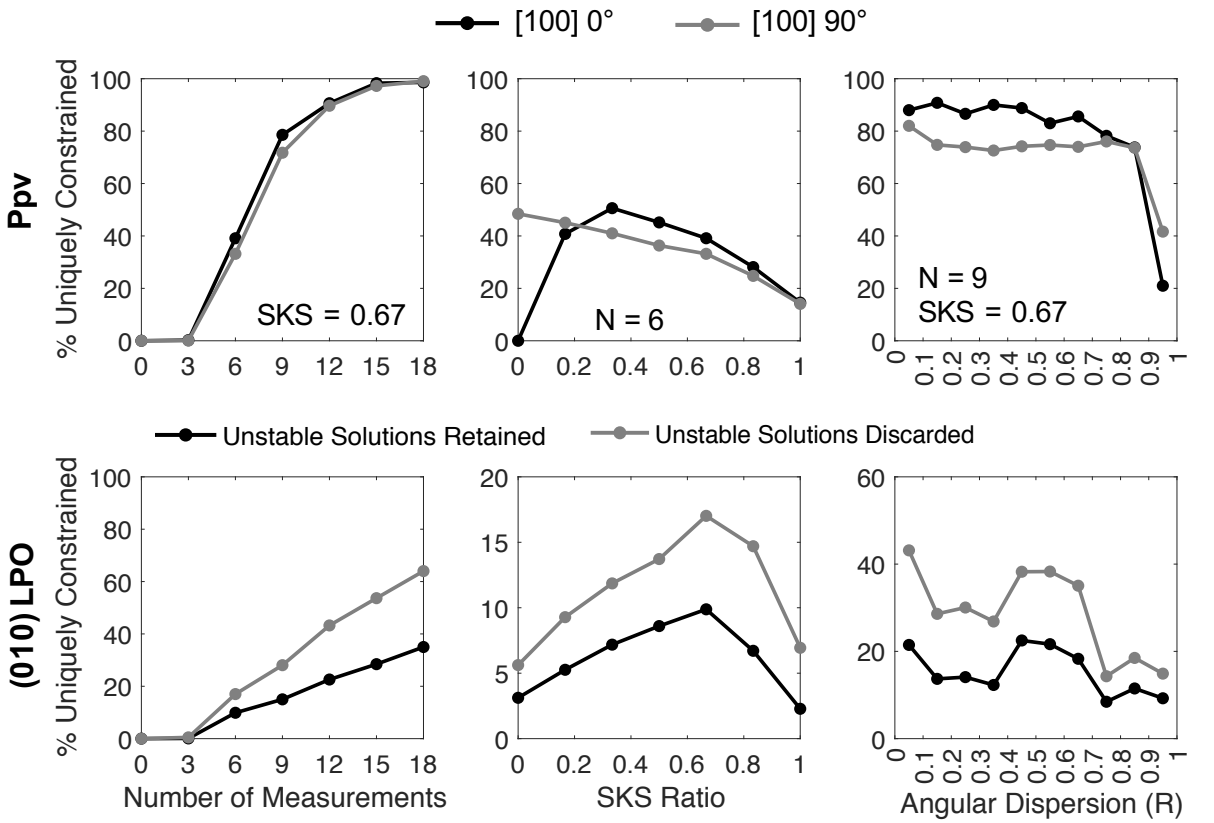

(b) Adding 1 Reflection Measurement

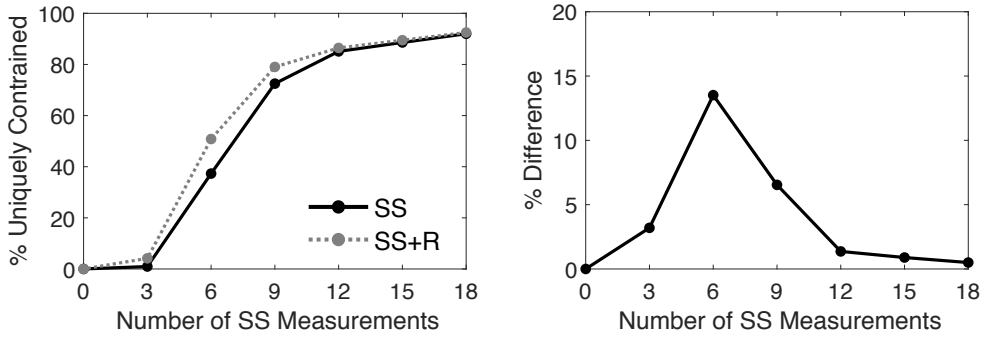

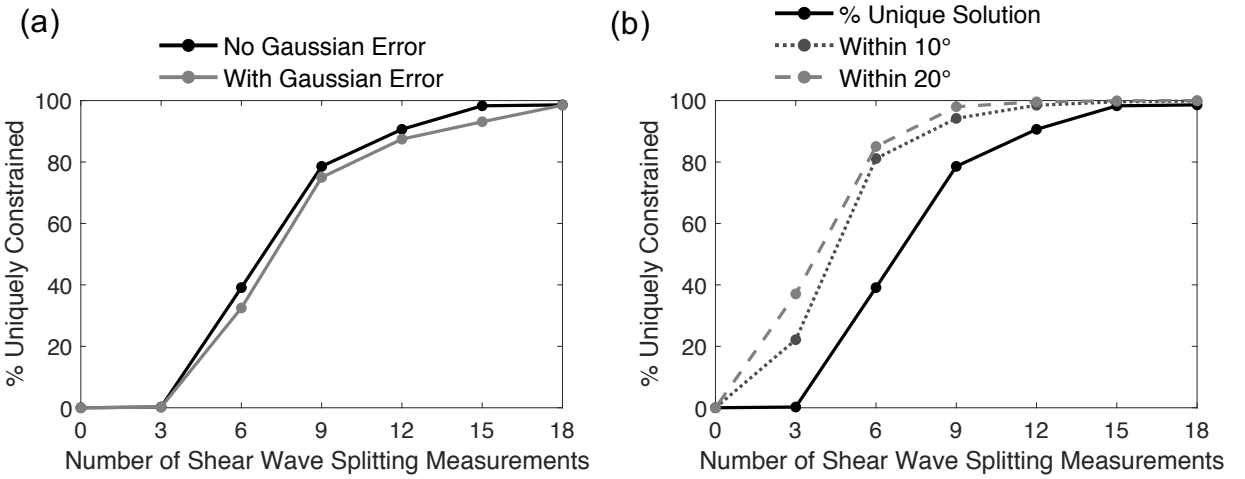
(a)
No Gaussian Error
With Gaussian Error
% Uniquely Constrained
Number of Shear Wave Splitting Measurements
0
20
40
60
80
100
0
3
6
9
12
15
18
(b)
% Unique Solution
Within 10°
Within 20°
% Uniquely Constrained
Number of Shear Wave Splitting Measurements

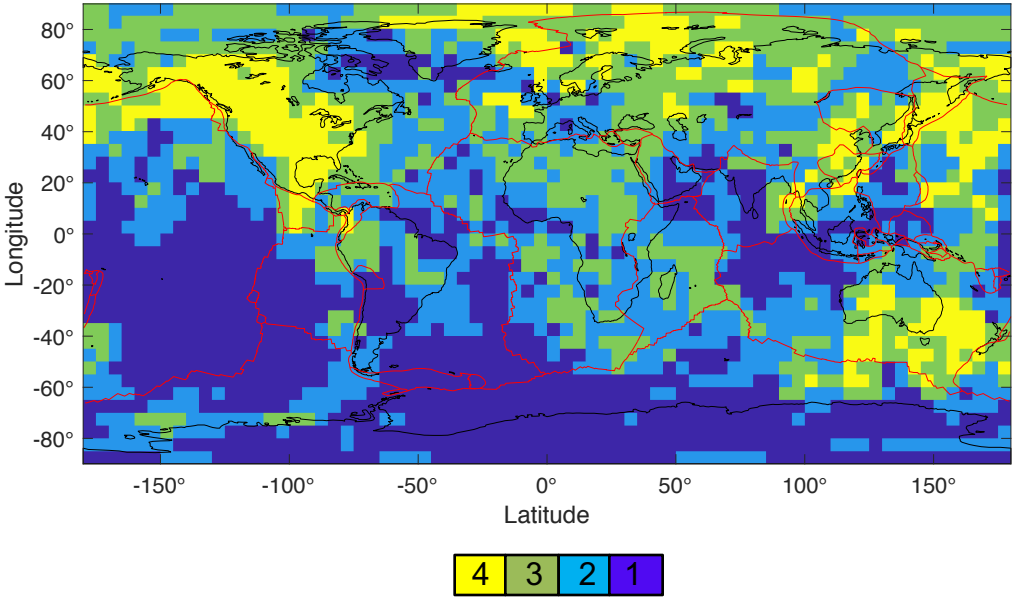
80°
60°
40°
20°
0°
-20°
-40°
-60°
-80°
Longitude
-150°
-100°
-50°
0°
50°
100°
150°
Latitude
4
3
2
1

Supplemental Material:

Constraining lowermost mantle anisotropy with body waves: A synthetic modeling study

Neala Creasy[1*], Angelo Pisconti[2], Maureen D. Long[1], Christine Thomas[2], and James Wookey[3]

[1]Department of Geology and Geophysics, Yale University
[2]Institut für Geophysik, Universität Münster
[3]Department of Earth Sciences, University of Bristol
*Corresponding author. Email: neala.creasy@yale.edu

Supplement Figures

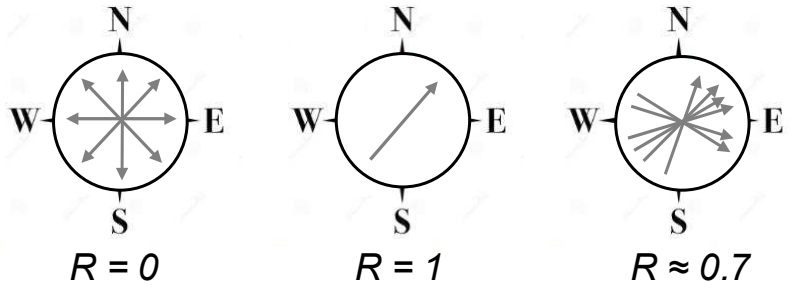

Figure S1. Schematic diagram showing the definition of angular dispersion (R), with arrows indicating a direction anywhere from 0° to 360°. Small values of *R* indicate a wide distribution of directions, while larger values indicate a tight configuration.

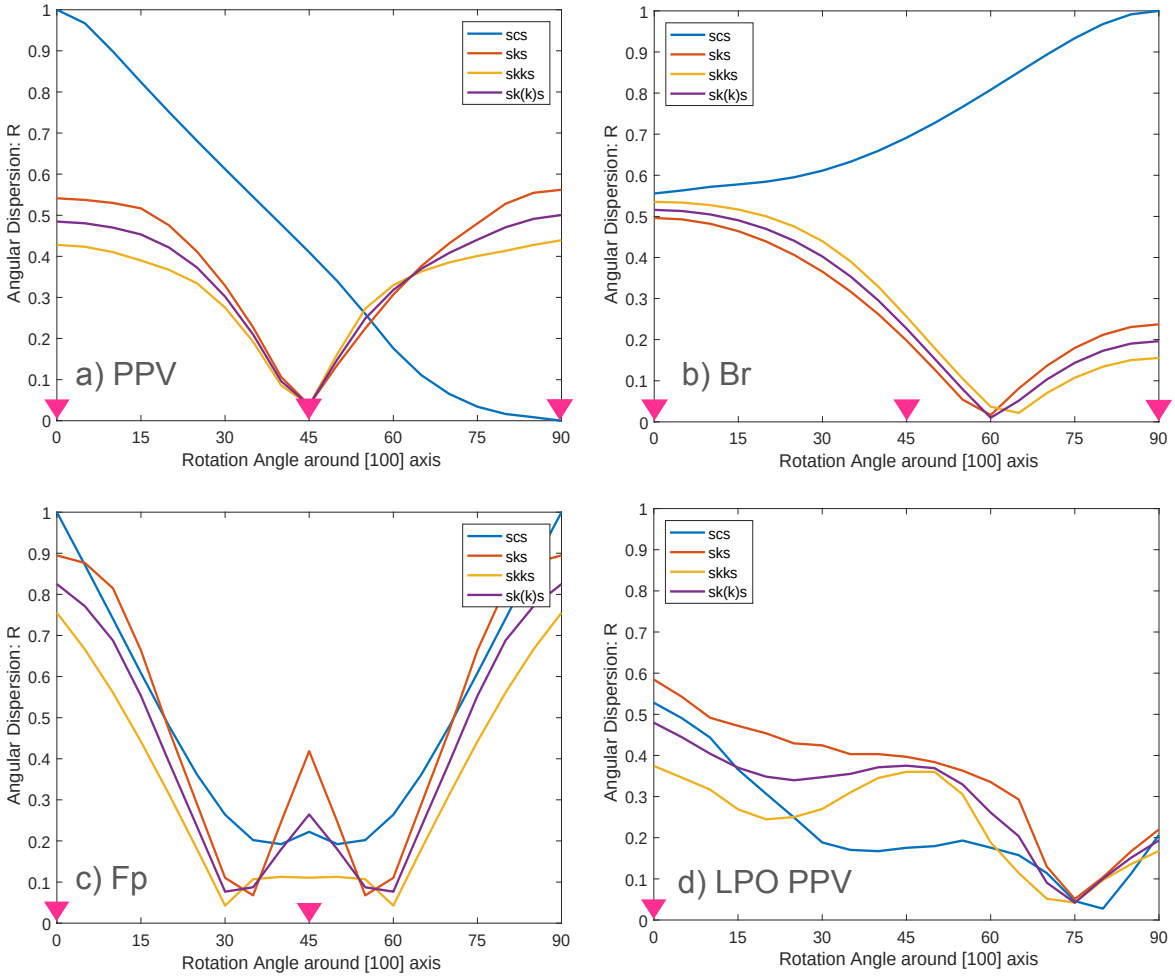

Figure S2. Angular dispersion – R – plots of all predicted fast axis directions for SKS (red), SKKS (orange), SKS and SKKS (violet), and ScS (blue). Equations (2) and (3) from the main text were used to calculate R; however, since fast axis directions can only vary from -90° to 90°, the fast axis orientations were adjusted from -90 to 90 to 0 to 360. Angular dispersion is plotted in terms of the clockwise rotation angle about the [100] axis of (a) post-perovskite (PPV), (b) bridgmanite (Br), (c) ferropericlase (Fp), and (d) LPO of PPV of the given models, respectively. Magenta triangles indicate the starting models' orientations used in the modeling in the main text as in Figures 8 and 9.

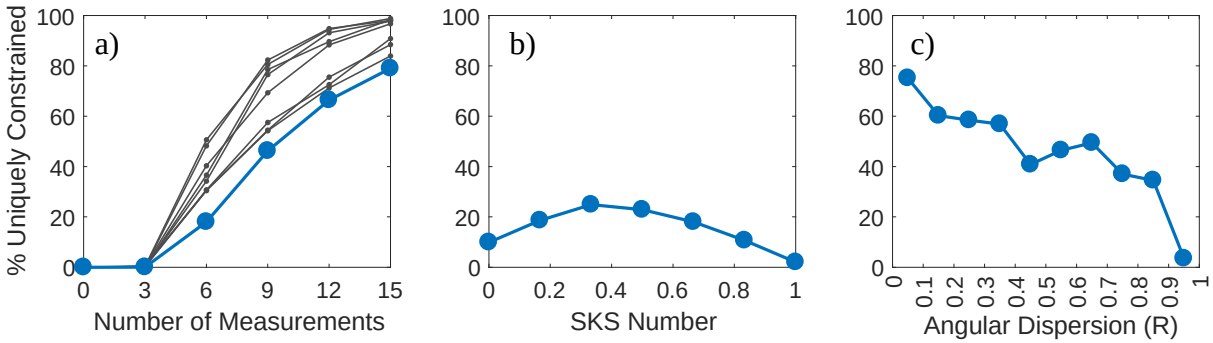

Figure S3. Results of synthetic tests that aim to uniquely constrain the orientation of a Ppv starting model, as discussed in section 3.3 in the main text, by selecting 9 random the starting orientations of the Ppv tensor. Each figure illustrates the probability of uniquely identifying the given starting model's orientation using the synthetic data, for nine different orientations of Ppv. As in Figure 7, each column represents the variable that was allowed to vary, while the other two were fixed. For (a), the SKS number was fixed (0.67). For (b), the number of measurements was fixed to six. For (c), the number of measurements was fixed to nine measurements and an SKS number of 0.67. The blue lines in (b) and (c) correlate to the blue line in (a), where the variation of SKS number and angular dispersion were only tested for one of the starting model orientations.

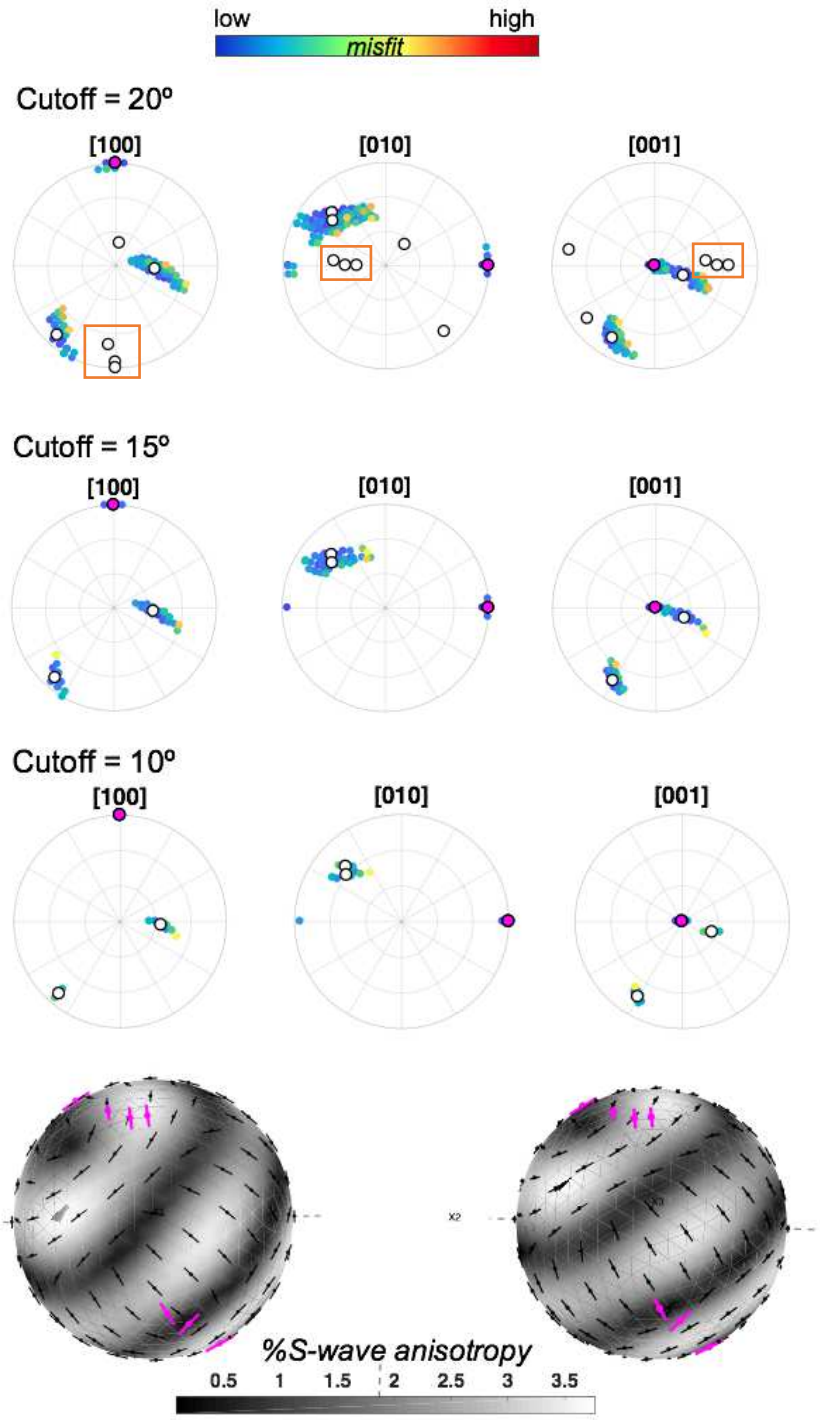

Unstable solution

Unstable solution rotated by 5 degrees, which fails the misfit criterion

Figure S4: Example illustrating the identification of unstable solutions in a test that aimed to identify the starting orientation of a horizontal textured Ppv LPO. The polar plots show all possible orientations that fit a given synthetic dataset. The colors represent misfit values. The white circles mark the minimum misfit of each cluster of possible orientations. The magenta circles show the correct solution. The orange boxes highlight some of the unstable solutions. Each row represents a different misfit cutoff. The top row represents the cutoff used in this study (20°). The second row uses a cutoff of 15° and the third row 10°. With a lower cutoff, the unstable solutions are eliminated. The bottom elastic tensors on the left show and example of one of the resulting unstable solution from the orange boxes in the first row. The elastic tensor on the right show the same tensor but rotated by 5°, which fails the misfit criterion. The magenta lines represent the measurements used in this simulation. Colors here represent %S wave anisotropy.